

WIDE BINARIES FROM GAIA DR3 : TESTING GR VS MOND WITH REALISTIC TRIPLE MODELLING

C. PITTORDIS, W. SUTHERLAND, AND P. SHEPHERD

School of Physical and Chemical Sciences, Queen Mary University of London, Mile End Road, London E1 4NS, UK.

(Dated: Accepted by Open Journal of Astrophysics - 2025 July 29)

Version 2025 July 30

ABSTRACT

We provide an updated test for modifications of gravity from a sample of wide-binary stars from *Gaia* DR3, and their sky-projected relative velocities. Here we extend on our earlier 2023 study, using several updated selection cuts aimed at reducing contamination from triple systems with an undetected third star. We also use improved mass estimates from *Gaia* FLAME, and we add refinements to previous modelling of the triple and other populations and the model-fitting. We fit histograms of observed vs Newtonian velocity differences to a flexible mixture of binary + triple populations with realistic eccentricity distributions, plus unbound flyby and random-chance populations. We find as before that Newtonian models provide a significantly better fit than MOND, though improved understanding of the triple population is necessary to make this fully decisive. .

1. INTRODUCTION

A number of recent studies have analysed relative velocities of very wide binary stars in *Gaia* DR3 to attempt to discriminate between GR + dark matter models and modified-gravity MOND-like models (see Famaey & McGaugh (2012) for a review of MOND models). This wide-binary test is potentially powerful, since dark-matter models predict that wide-binary stars should contain negligible dark matter and thus be entirely Newtonian, whereas MOND-like models predict increased accelerations leading to faster relative velocities at scales where the internal accelerations are below the MOND characteristic acceleration scale $a_0 \simeq 1.2 \times 10^{-10} \text{ m s}^{-2}$. This acceleration occurs at separation $\simeq 7 \text{ kAU}$ for a binary of $1 M_\odot$ total mass, while there is a smooth transition (with the details dependent on the specific version of MOND), so MOND predicts some deviations should be observable down to smaller separations $\sim 2 - 4 \text{ kAU}$. The first studies of this wide-binary test were by Hernandez et al. (2012b); Hernandez et al. (2012a); Hernandez et al. (2014), but these early studies were hampered by the limited precision of ground-based proper motion data. In our first paper in this series (Pittordis & Sutherland 2018, hereafter PS18) we used simulations to highlight the dramatic improvement then anticipated from the *Gaia* spacecraft (Gaia Collaboration et al. 2016). This was followed by our selection of wide binaries observed in *Gaia* DR2 (Pittordis & Sutherland 2019, hereafter PS19): that study revealed a “long tail” of apparent binaries with relative velocities well above expectations from either GR or MOND, and (Clarke 2020) suggested a likely explanation was triple systems with an unresolved or unseen third star perturbing the velocity of its close companion; this induces an additional term

which is the relative velocity between the photocentre and the barycentre of the close binary, which often dominates over the relative velocity between the distant star and the barycentre of the close binary. The model of formation of wide binaries by Kouwenhoven et al. (2010) provides some support to this, predicting that a fairly substantial fraction of observed wide “binary” systems should actually be triples or quadruples with close inner system(s).

More recently, a number of wide-binary studies have been done using *Gaia* EDR3 and DR3, with contrasting results: Hernandez et al. (2022) and Hernandez (2023) analysed relatively small samples with stringent data-quality cuts and claim evidence for a MOND signal. Also Chae (2023) and Chae (2024) have selected larger samples and also claim evidence for a MOND signal. Conversely, Pittordis & Sutherland (2023, hereafter PS23) fitted a mixed model of binaries, triples and flyby systems to their own sample of wide binary candidates, and found a significant preference for GR over MOND. Also Banik et al. (2024) used a subset of the PS23 binary sample, and used a sophisticated likelihood-modelling based on a large library of binary and triple orbits, and also found that GR was preferred over MOND at high significance.

These apparently contradictory results appear to originate from differences in sample selection, statistical methods and/or modelling of triple systems, with the triple systems perhaps the dominant source of uncertainty.

Fortunately for future prospects, a study by Manchanda et al. (2023) showed that a high fraction $\sim 85\%$ to 95% of unseen triple systems can be flagged by combining a variety of followup methods, including future *Gaia* multi-epoch astrometry, and followup speckle-imaging and coronagraphic observations; a key conclusion from Manchanda et al. (2023) is that nearly all main-sequence third stars are detectable in principle: third stars closer

E-mail: cp.pittordis@gmail.com
E-mail: w.j.sutherland@qmul.ac.uk
E-mail: p.d.shepherd@qmul.ac.uk

than $\lesssim 25$ AU can largely be detected by astrometric accelerations in *Gaia* data, while third stars at separations $\gtrsim 20$ AU are detectable by speckle and/or coronagraphic imaging. However, this scenario requires both the full 10-year mission *Gaia* data (DR5 projected for 2030) and substantial telescope time for followup imaging, so is a long-term prospect. In the short term it is desirable to revisit the gravity test based on the available *Gaia* DR3 data, which is the purpose of this paper.

This paper is essentially an updated version of [Pitordis & Sutherland \(2023\)](#) with several improvements aimed mainly at reducing the fraction of triple systems via data cuts, more realistic modelling of the triple population, and an improved fitting procedure; The main refinements are the following:

- i) A tighter cut on the `ruwe` parameter,
- ii) A new cut against triple systems using the “Lobster” diagram,
- iii) Improved stellar mass estimates using the *Gaia* FLAME data,
- iv) Several enhancements to the model triple distribution.
- v) Analysing a wider range of projected separations extending down into the quasi-Newtonian regime,
- vi) An improved fitting procedure with a variable triple fraction, while distributions of unbound systems are constrained to have a realistic distribution of projected separation.

The plan of the paper is as follows: in Section 2 we describe the sample selection and the refinements compared to PS23. In Section 3 we review some statistical properties of the \tilde{v} parameter used later, and describe the modelling of triple and other populations; and in Section 4 we fit the observed \tilde{v} histograms as a mixture of binary, triple and flyby populations from either GR or MOND orbit simulations. We summarise our conclusions in Section 5.

2. *Gaia* DR3 BINARY SAMPLE SELECTION AND FLAME MASSES

2.1. Preliminary selection

Our starting point is the public *Gaia* Data Release 3 dataset (DR3), ([Gaia Collaboration et al. 2023](#); [Creevey et al. 2023](#)) released on 2022 June 13, joined with the Final Luminosity Age Mass Estimator (FLAME) data ([van Leeuwen et al. 2022](#)). We initially select all stars with measured parallax $\omega > \frac{10}{3}$ mas (i.e. estimated distance < 300 pc) with a *Gaia* broadband magnitude $G < 17$, and cutting out the Galactic plane with absolute latitude $|b| \leq 15$ deg, yielding a preliminary DR3 sample of 2,102,657 stars (hereafter PDR3). The ADQL query used is given in the Appendix. Star data-quality cuts are applied at a later stage, in order that these may be adjusted after the initial selection.

We then applied a similar search method as described in section 2 from [PS19](#) and [PS23](#) to PDR3, to search this nearby-star sample for pairs of stars with projected separation ≤ 50 kAU (calculated at the mean distance of

each candidate pair), and distances consistent with each other within $4\times$ the combined uncertainty (with an upper limit of 8 pc) i.e. $|d_1 - d_2| \leq \min(4\sigma_d, 8 \text{ pc})$, and projected velocity difference $\Delta v_p \leq 5 \text{ km s}^{-1}$ as inferred from the difference in proper motions; here, the projected velocity difference is computed assuming *both* stars in each candidate pair are actually at the mean of the two estimated distances. (Note here, this 5 km s^{-1} velocity difference is enlarged from the 3 km s^{-1} used by [PS23](#), to avoid incompleteness for the high-velocity tail of systems at smaller projected separations, down to 1.25 kAU analysed below).

This search results in a first-cut sample of 97,505 candidate DR3 wide binaries, including FLAME masses where available (hereafter WB-DR3-FLAME).

2.2. Additional cuts

This sample is then pruned using the same additional cuts as section 2.2 - 2.5 of [PS23](#), for removing moving groups; known open clusters; systems with a fainter nearby companion at $G < 20$ and parallax consistent with equal distance; and a cut on the u parameter in Eq. 1 of [PS23](#). This reduces the WB-DR3-FLAME sample to 75,501 candidates.

Additional cuts are applied to this sample based on the “Renormalised Unit Weight Error” or `ruwe` parameter defined in *Gaia* DR3: this is a measure of scatter of single-epoch *Gaia* observations around the basic 5-parameter fit parallax + uniform proper motion, rescaled by a factor dependent on magnitude and colour so the median `ruwe` for single stars is close to 1. Objects with a `ruwe` value significantly larger than 1 are indicative of excess scatter which may indicate a poor fit or astrometric wobble from an unresolved close binary. The studies by [Belokurov et al. \(2020\)](#) and [Fitton et al. \(2022\)](#) analysed the *Gaia* `ruwe` value for single stars, and show an increased probability of binarity at `ruwe` > 1.2 ; therefore we apply an additional cut that both stars in a candidate binary are required to have `ruwe` < 1.2 : note that this is more restrictive than the `ruwe` < 1.4 used in [PS23](#).

In addition, we also apply a cut based on the “Image Parameters Determination of Multiple Peaks”, the parameter `ipd_frac_multi_peak` defined in *Gaia* DR3; this parameter provides information on the raw windows used for the astrometric processing of this source from the Image Parameters Determination (IPD) module in the core processing. It is defined as the integer percentage of windows (having a successful IPD result), for which the IPD algorithm has identified a double peak, meaning that the detection may be a visually resolved double star (either just visual double or real binary). The study by [Tokovinin \(2023\)](#), comparing nearby hierarchical systems with *Gaia* and speckle interferometry, indicates that resolved pairs have values `ipd_frac_multi_peak` > 2 . Therefore, we apply a cut that both stars in our candidate wide binary have `ipd_frac_multi_peak` ≤ 2 . (Small positive values of 1 or 2 may occur for single stars from an occasional cosmic-ray hit etc, and are accepted).

After both cuts `ruwe` < 1.2 and `ipd_frac_multi_peak` ≤ 2 , our WB-DR3-FLAME sample is reduced to 40,116 candidate wide binaries.

2.3. Mass Estimates using FLAME

In the preliminary selection A creating the PDR3, only $\sim 35\%$ of the stars have an estimated FLAME mass. In our WB-DR3-FLAME binaries, only 17% have a FLAME mass for both stars, while 62% have a FLAME mass for at least one star. For our gravity test below, we require a mass estimate for each binary candidate, hence we estimate masses for the stars lacking FLAME masses via a combination of the sample from Pecaut & Mamajek (2013) and the populated FLAME mass candidates. We begin by adopting the main-sequence $M_I(\text{mass})$ relation of *Version 2021.03.02* from Pecaut & Mamajek (2013) for the mass range $0.18 \leq M/M_\odot \leq 2.0$, and the $V - I, M_I$ colour relation from the same, where M_I denotes I-band absolute magnitude. We then apply the colour relation given in Table C2 (i.e., Johnson-Cousins relation) of Riello et al. (2021) to predict G magnitude from V and I magnitudes as

$$G \simeq V - 0.01597 + 0.02809(V - I) - 0.2483(V - I)^2 + 0.03656(V - I)^3 - 0.002939(V - I)^4 \quad (1)$$

to obtain a sub-dataset (hereafter; *PM-GMag-Mass*) of absolute *Gaia* magnitude, M_G , and mass, in mass range $0.18 \leq M/M_\odot \leq 2.0$ as above. Next, for each star in WB-DR3-FLAME we compute M_G directly from G and parallax distance, then generate a sub-dataset (hereafter; *PS-DR3-FLAME-GMag-Mass*) of *Gaia* magnitude M_G and FLAME masses. This follows from joining the two sub-datasets *PM-GMag-Mass* and *PS-DR3-FLAME-GMag-Mass* into one. From this sample, we fit the mass/ M_G relation for the mass range as above with a 6th order polynomial,

$$\log_{10}(M/M_\odot) = \sum_0^6 b_n M_G^n \quad (2)$$

giving coefficients $b_0 \simeq 0.505$, $b_1 \simeq -0.125$, $b_2 \simeq -0.0140$, $b_3 \simeq 6.97 \times 10^{-3}$, $b_4 \simeq -9.33 \times 10^{-4}$, $b_5 \simeq 5.53 \times 10^{-5}$, $b_6 \simeq -1.38 \times 10^{-6}$. We then use equation 2 to estimate the masses of the stars without FLAME mass estimates from their M_G absolute magnitudes.

2.4. Lobster diagram cuts

Here, we apply a further cut to our WB-DR3-FLAME sample using the *Lobster Diagram* technique. This follows the method introduced by Hartman et al. (2022), where they cross-matched & examined *Gaia*, SUPERWIDE, TESS, K2 and Kepler data, producing a technique to distinguish between “pure” wide binaries with exactly 2 stars, and triples where one component of the WB is an unresolved close binary: The method involves computing for each star the difference between observed absolute magnitude, and that predicted from a main-sequence colour-magnitude relation: each wide-binary then produces a point on a 2D plot, called the “Lobster diagram” by Hartman et al. (2022). Since deviations from the main-sequence ridgeline due to age and metallicity variation are highly correlated for both stars in a WB, pure 2-star WBs populate a thin diagonal stripe at 45 degrees (the lobster “body”); while a luminous third star produces deviations off this line by up to 0.75 mag. These triple systems populate a pair of “lobster claws” in

the plot (see Fig 7 of Hartman et al. 2022); which claw is occupied depends on which one of the wide pair is the close binary.

We begin by creating our sub-dataset from Pecaut & Mamajek (2013) for the mass range $0.18 \leq M_\odot \leq 2.0$ to include colours $B_p - R_p \leq 3.0$ i.e., for F, G, K, M Stars, and compute the absolute *Gaia* magnitude M_G magnitude from V and I , using the Johnson-Cousins relation 1. Next, we fit a 5th order polynomial to the M_G/colour relation as

$$M_{G,\text{poly}} = \sum_0^5 c_n u^n \quad (3)$$

where $u \equiv B_p - R_p - 1.4$, defined so the range in u is roughly symmetric around zero. The resulting fit coefficients are $c_0 \simeq 6.997$, $c_1 \simeq 3.229$, $c_2 \simeq -1.282$, $c_3 \simeq 0.608$, $c_4 \simeq 0.473$, $c_5 \simeq -0.269$.

Given this polynomial, we select binaries from the WB-DR3-FLAME sample where both stars are in the colour range $0.068 \leq B_p - R_p \leq 3.16$, then construct a “lobster” diagram following Hartman et al. (2022): for each star in each candidate binary, we define ΔM_G as the difference between observed M_G and the fit-line at the observed colour, i.e.

$$\Delta M_G \equiv M_{G,\text{obs}} - M_{G,\text{poly}} \quad (4)$$

Plotting $\Delta M_{G,1}$ vs $\Delta M_{G,2}$ for both stars in each binary system gives a lobster plot shown in Figure 1.

Next, we take values of the two over-luminosity columns $\Delta M_{G,1}, \Delta M_{G,2}$ and create a matrix array, and feed this into a Density-Based Spatial Clustering of Applications with Noise (DBSCAN) machine-learning algorithm, where this algorithm is accessed via python package scikit-learn Pedregosa et al. (2011), where the DBSCAN algorithm is developed by Ester et al. (1996) and Schubert et al. (2017). DBSCAN finds core samples of high density and expands clusters from them. This is ideal for datasets that contain clusters of similar density, in our case, trying to separate the *lobster-body* cluster from the WB-DR3-FLAME dataset itself. After inspecting multiple parameters for our DBSCAN model and analysing their results, the parameters that provided a good model for the lobster-body from our sample are;

$$\begin{aligned} \text{LobsterBody} = \text{DBSCAN}(\quad \\ \text{eps} = 0.08, \\ \text{min_samples} = 160, \\ \text{metric} = \text{manhattan}) \quad (5) \end{aligned}$$

Where **eps** is the maximum distance between two samples (e.g., values from $\Delta M_{G,1}$ and $\Delta M_{G,2}$) for one to be considered as in the neighbourhood of the other, *min_samples* is the number of samples in a neighbourhood for a point to be considered as a core point. This includes the point itself. If *min_samples* is set to a higher value, DBSCAN will find denser clusters, whereas if it is set to a lower value, the found clusters will be more sparse. The *metric* is the method used to calculate the distances between points, we chose ‘*manhattan*’ over ‘*euclidean*’, as it provided a better lobster-body result, also the ‘*manhattan*’ distance helps with reducing the impact of extreme outlier values, and provided faster processing of Density Based Clustering. The results of the selection Eq. 5 are shown in Figure 1.

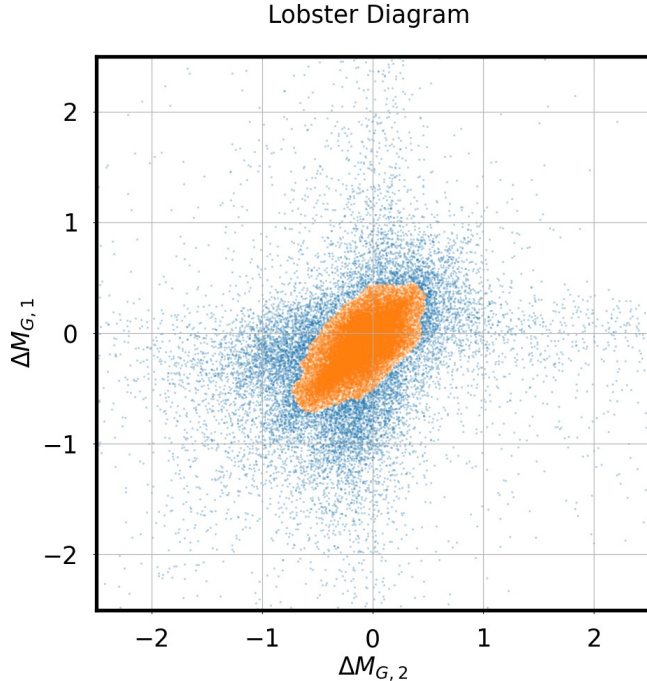


FIG. 1.— Scatter plot comparing the ΔM_G parameter of Eq. 4 for Star 1 & Star 2 (ordered by ascending declination) of each wide binary system. The panel shows the full 40,116 candidates prior to the Lobster cut; the orange points are the subsample of 23,223 candidates selected by Eq. 5

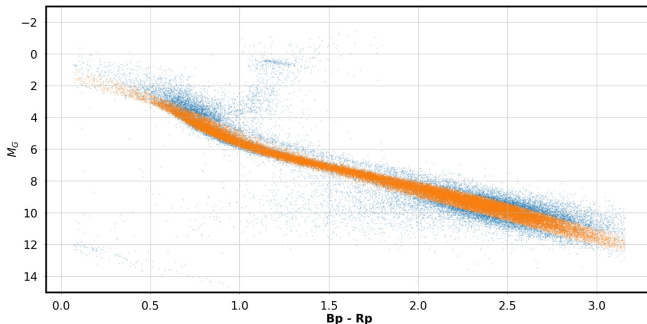


FIG. 2.— Colour-magnitude diagram of M_G absolute magnitude vs $B_P - R_P$ colour; for both stars in each WB candidate. Blue points fail the lobster cut, orange points pass the lobster cut.

We then select the subset of WB-DR3-FLAME binary candidates with values of $(\Delta M_{G,1}, \Delta M_{G,2})$ within the lobster-body defined above. This reduces the sample to 23,223 wide-binary candidates; as this is the final part of our data cleaning, this sample is now our ‘Cleaned’ WB-DR3-FLAME (CWB-DR3-FLAME); this is the sample used exclusively in subsequent analysis. The colour-magnitude diagram for both stars in these candidates is shown in Figure 2, showing that the lobster cut removes stars on the upper side of the main sequence, and also removes a number of white dwarfs and subgiants, leaving a clean main sequence population. Our wider colour range and presence of white dwarfs and subgiants explains why our lobster diagram Figure 1 has more outliers compared to Hartman et al. (2022) which used more pre-selection cuts; but our lobster-body selection still gives a rather clean main sequence in Figure 2.

2.5. Results and scaled velocities

For the surviving 23,223 candidate binaries above, we show a plot of projected velocity difference vs projected separation in Figure 3; similar to PS23, this shows a clear excess at low Δv_p approximately as expected for bound binaries, with an overdense cloud following a locus $\Delta v_p \sim 1 \text{ km s}^{-1} (r_p / 1 \text{ kAU})^{-0.5}$.

The population above the dense cloud is slightly sparser than the corresponding figure in PS23, indicating that the additional cuts are probably successful at removing many but not all higher-order multiples. It is also notable that the points become sparser towards the top of the diagram at $\Delta v_p > 2.5 \text{ km s}^{-1}$, except in the upper right corner at $r_p \gtrsim 30 \text{ kAU}$ so $\log_{10} r_p \gtrsim 4.48$ in Figure 3; random pairs would produce the opposite trend, increasing with Δv_p due to phase-space volume; this supports our conclusion below that random or unbound pairs are only a small contribution at $r_p < 20 \text{ kAU}$, and the high-velocity tail is likely dominated by triple/quadruple systems.

It is more informative to rescale to the typical Newtonian orbit velocity, so next we use the estimated masses described in 2.3.

As in PS23 for each candidate binary we then define

$$v_c(r_p) \equiv \sqrt{GM_{tot}/r_p} \quad (6)$$

as the Newtonian circular-orbit velocity at the current *projected* separation; and we then divide the measured projected velocity difference by the above to obtain a dimensionless ratio

$$\tilde{v} \equiv \frac{\Delta v_p}{v_c(r_p)}. \quad (7)$$

This \tilde{v} parameter is becoming commonly used in the recent literature, e.g. PS23, Banik et al. (2024), Chae (2024). By construction in standard gravity, $\tilde{v} = 1$ for a face-on circular orbit, and $\tilde{v} < \sqrt{2}$ for a bound pure binary; also the median $\tilde{v} \sim 0.6$ for random inclinations due to projection factors; see the following Section 3.1 for details. A scatter plot of \tilde{v} vs r_p for our cut sample is shown in Figure 4, and histograms of this ratio in bins of r_p are compared with models below in Section 4.

2.6. Transverse velocity errors

We have estimated relative-velocity errors assuming uncorrelated errors between the two components of the binary, simply from the root-sum-square of the quoted rms errors in μ_α and μ_δ for each of the two stars in each binary, and multiplying by mean distance to obtain the transverse-velocity error. (This should be reasonable as long-range correlated errors should mostly cancel between the two stars). Parallax errors are ignored here as these contribute a multiplicative error $\lesssim 1\%$ to Δv_p , much smaller than the additive errors from proper-motion uncertainty.

Table 1 shows the comparison of the transverse velocity random errors between the CWB-EDR3 and CWB-DR3-FLAME. We can see using the FLAME masses and the extra ‘Lobster Body cut’ has made a small improvement, with the median at an impressively small value of $\sigma(\Delta v_p) \approx 0.04 \text{ km s}^{-1}$. When converting to the ratio

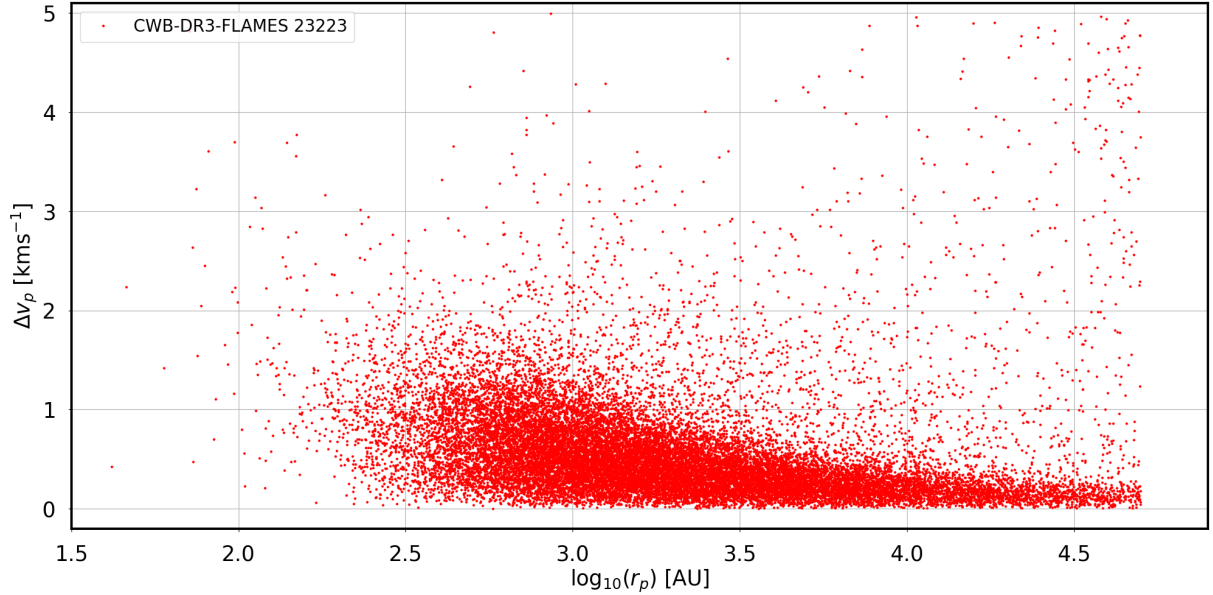


FIG. 3.— Scatter plot of projected relative velocity Δv_p (y-axis) vs projected separation (log scale, x-axis) for the CWB-DR3-FLAME binary candidates. The main selection cuts are visible at top and right.

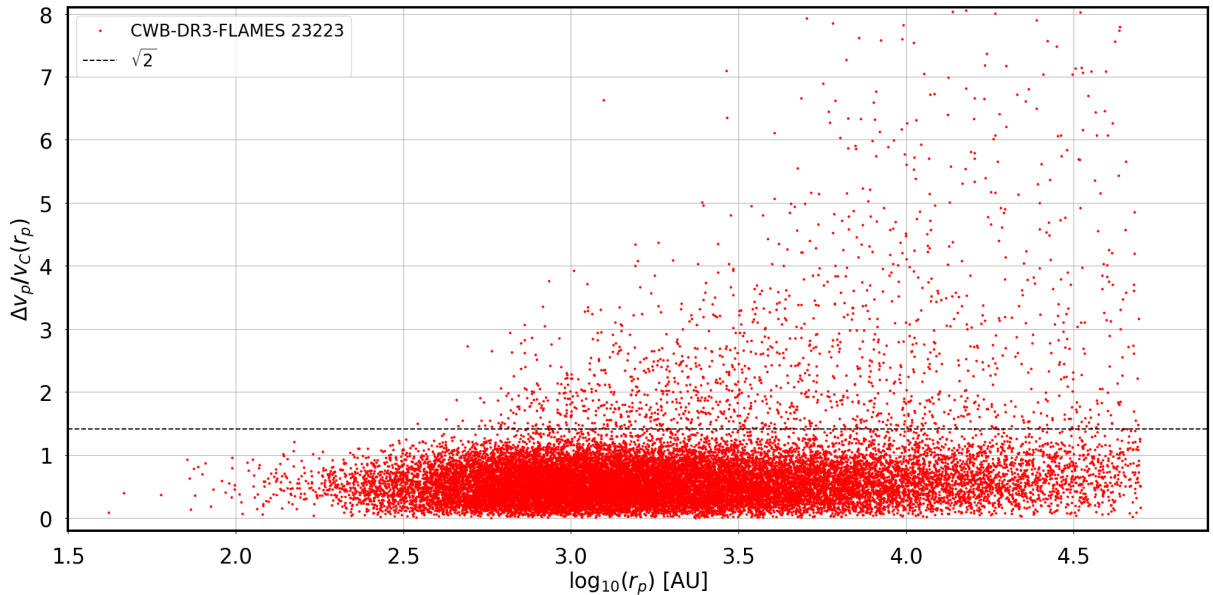


FIG. 4.— Scatter plot of projected velocity relative to Newtonian, \bar{v} from Eq. 7, vs projected separation for CWB-DR3-FLAME sample. The dashed line at $\sqrt{2}$ indicates the Newtonian limit. The upper Δv_p cutoff now becomes a diagonal curve, causing the empty region at upper left, but this border is not sharp due to the additional dependence of \bar{v} on mass. Note that in later analysis we only use the sample at $r_p > 1.25$ kAU so $\log_{10} r_p > 3.09$, so incompleteness in the upper-left region is unimportant.

to circular-orbit velocity $\sigma(\Delta v_p)/v_c(r_p)$, we see a negligible difference between the data sets. However, when reducing to the “wide” subsample with $5 < r_p < 20$ kAU, the values reduce by on average ~ 0.1 , with a median reduced to 0.08 and the 80th percentile is 0.16. A scatter plot of $\sigma(\Delta v_p)$ versus distance is shown in Figure 5; the trend with distance is clear, but most systems have $\sigma(\Delta v_p) \lesssim 0.1 \text{ km s}^{-1}$ even near our 300 pc distance limit.

The latter values are significantly smaller than 1, but not very small, so the effect of random proper motion errors will affect the detailed shape of the distributions below. However, in future *Gaia* data releases these values

are expected to reduce by factors of at least 2–4 as proper motion precision scales as $\propto t^{-3/2}$ for fixed scan cadence, so the random errors in proper motions are likely to become relatively unimportant in the medium-term future.

We note that for a “typical” binary below at $r_p \sim 5$ kAU and $d \sim 200$ pc, the angular separation is 25 arcsec, so these are very well resolved and the uncertainty on r_p is essentially the same as the error on the mean distance, typically below 1 percent and almost negligible. The error on Δv_p is dominated by random measurement errors on the proper motions, assuming that correlated systematic errors mostly cancel between the two com-

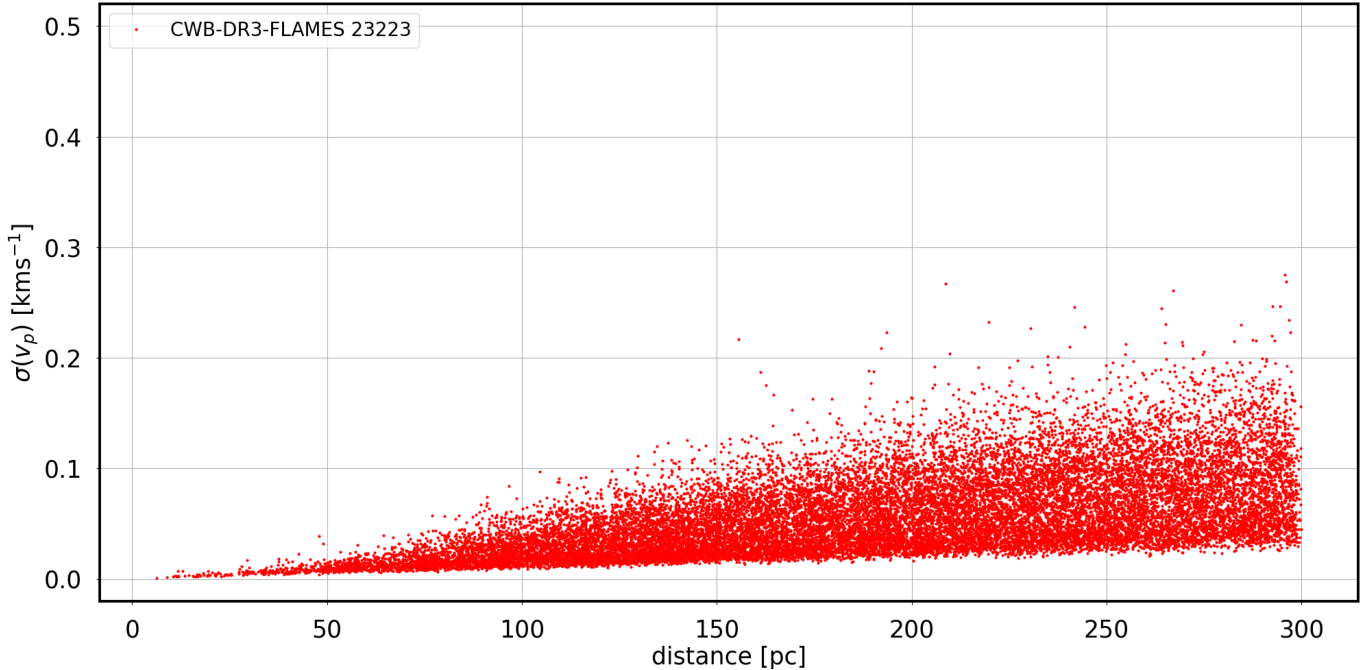


FIG. 5.— Scatter plot of rms velocity uncertainty $\sigma(\Delta v_p)$ versus mean distance for candidate binaries in CWB-DR3-FLAME.

TABLE 1

TABLE COMPARING PERCENTILES OF TRANSVERSE VELOCITY ERRORS AND RELATIVE TO CIRCULAR VELOCITY, BETWEEN CWB-EDR3 (PS23) AND CWB-DR3-FLAME DATA SETS. UPPER TABLE FOR THE FULL SETS, LOWER TABLE FOR SUBSAMPLE WITH $5 < r_p < 20$ kAU.

All r_p	CWB-EDR3	CWB-DR3-FLAME
$\sigma(\Delta v_p)$ [km s ⁻¹] (50%, 80%, 90%)	$\approx [0.06, 0.1, 0.13]$	$\approx [0.04, 0.08, 0.1]$
$\sigma(\Delta v_p)/v_c(r_p)$ (50%, 80%, 90%)	$\approx [0.06, 0.12, 0.19]$	$\approx [0.06, 0.13, 0.2]$
$(5 < r_p < 20$ kAU)	CWB-EDR3	CWB-DR3-FLAME
$\sigma(\Delta v_p)$ [km s ⁻¹] (50%, 80%, 90%)	$\approx [0.05, 0.09, 0.11]$	$\approx [0.05, 0.08, 0.1]$
$\sigma(\Delta v_p)/v_c(r_p)$ (50%, 80%, 90%)	$\approx [0.14, 0.26, 0.34]$	$\approx [0.08, 0.16, 0.23]$

ponents of each binary. Since we are mostly interested in statistical distributions, the effect of random errors is modest as long as these are not larger than ~ 0.2 in \tilde{v} . Note that for systems with small observed ratios $\tilde{v} \sim 0.4$, the *fractional* uncertainty in this ratio is rather large; however such systems still have a high probability of the true ratio being $\lesssim 0.8$, so this scatter is relatively unimportant. In the following fitting, it will turn out that the distribution between $0.8 \lesssim \tilde{v} \lesssim 1.5$ is the most important discriminant between gravity models: for these systems, the fractional uncertainty is relatively modest. We include simulated proper-motion noise errors in our model

binary & triple orbits as described below; this follows the recommendation of [Hernandez et al. \(2024a\)](#).

While a possible tail of non-Gaussian errors in the *Gaia* data remains a slight concern, this should improve in future *Gaia* releases as more observing epochs become available to reject outliers. The precision will continue to increase with future DR4 and beyond in the extended mission, so *Gaia* random errors will become negligible compared to other sources of uncertainty (especially contamination from triple systems, see below).

3. ORBIT SIMULATIONS FOR \tilde{v} DISTRIBUTIONS

Our main analysis below consists of fitting the joint distribution of candidate binaries in the (r_p, \tilde{v}) plane seen in Figure 4 to a mixture of simulated binary, triple and other populations; below we will consider binaries in the range $1.25 \text{ kAU} \leq r_p \leq 20 \text{ kAU}$. Here the lower limit ensures that angular separations of these WBs are ≥ 4 arcsec, so WBs are well resolved and minimising possible windowing effects in the *Gaia* data. For the upper limit, beyond 20 kAU there are fewer systems, perspective-rotation effects and proper-motion measurement errors become relatively larger, and binaries are more susceptible to disruption by encounters with other stars. The selected range spans internal accelerations from $\sim 30 a_0$ to $0.2 a_0$, so any MOND transition should be clearly observable, if present.

After binning, the observed histograms of \tilde{v} in r_p bins are fitted later to an adjustable mixture of simulated binary, triple and other populations; for the modelling, we construct simulated \tilde{v} histograms for separate populations of pure-binaries, pure triples, flybys and random projections; then in the fitting below, the shapes of \tilde{v} distributions for each population are held fixed at the simulation results, while the relative numbers of each population are adjusted to fit the data. In this section we summarise some properties of the \tilde{v} distribution for

Newtonian binaries in Section 3.1, then describe the parameters used to generate the model populations in the simulations in Sections 3.2 – 3.5.

3.1. Statistics of \tilde{v} for pure binaries

A useful property of \tilde{v} is that for pure binary systems and Newtonian gravity, its statistical distribution can be robustly predicted given an assumed eccentricity distribution $f(e)$, and the solid assumptions of random orbit orientations and random phases. (We note that if orbit orientations are non-random, they will likely correlate with the Galactic plane; since our sample covers a wide range of Galactic latitude $15^\circ < |b| < 90^\circ$, this should mostly wash out any Galactic alignment effects).

If we had access to 3D velocities and separations, we can define an analogous quantity $\tilde{v}_{3D} \equiv |\Delta\mathbf{v}|/v_c(r)$; as noted in PS18 this is simply given by $\tilde{v}_{3D} = \sqrt{2 - (r/a)}$. The cumulative probability distribution for \tilde{v}_{3D} is given by Eqs. 2 - 5 of PS18, and analytic expressions for the differential probability distribution are given by Benisty et al. (2023). However, in practice this 3D version is not usefully observable: radial velocity differences are measurable in principle, but very expensive in telescope time to reach the required precision $\lesssim 0.05 \text{ km s}^{-1}$ for a large sample, while the radial component of binary separation is essentially impossible to measure to the required kAU precision; so later we concentrate solely on the 2D \tilde{v} .

It was noted in PS18 that the 90th percentile of \tilde{v}_{3D} is close to 1.15 and is fairly robust against changing the eccentricity distribution $f(e)$; here we show that in 2D there is an analogous result for \tilde{v} , the numerical value is shifted downwards by projections since $\tilde{v} \leq \tilde{v}_{3D}$, but the 90th percentile of \tilde{v} is robustly close to 0.94 for a wide range of plausible eccentricity distributions.

In Figure 6 we show probability distributions for \tilde{v} for fixed values of e , and selected percentiles (1, 5, 10, 25, 50, 75, 90, 95, 99) of this distribution; this would be the result for a single binary of fixed e observed by many observers at random times and viewing angles. In practice we observe many binaries at a single time and viewing angle, and have no knowledge of e for any single binary, so the theoretical distribution is simply a sum of these weighted by a model for $f(e)$. Note that for low- e orbits there is a prominent caustic spike near 0.62; as in PS19 this corresponds to the maximum of \tilde{v} for nearly edge-on low- e orbits. As e increases, the spike broadens into a ramp, and a tail appears extending to a maximum value of $\sqrt{1+e}$. The mode of the distribution initially increases with e , then decreases sharply for high e , so high- e orbits produce many more systems at low $\tilde{v} \lesssim 0.4$, fewer at intermediate values $0.4 \lesssim \tilde{v} \lesssim 0.9$, but a similar number at $\tilde{v} > 0.9$. This is due to the well-known property that high- e orbits spend most of the time moving slower than average at $r > a$, and a small fraction of time moving faster than average at $r < a$. For the cumulative percentiles, note that the mean and median of \tilde{v} shift slightly downwards with increasing e ; the upper 95th and 99th percentiles increase with e as the tail population at $\tilde{v} > 1$ increases, while as in 3D the 90th percentile, \tilde{v}_{90} , is relatively insensitive to e ; considering the variation of \tilde{v}_{90} as a function of e , it shows a small roughly sinusoidal variation with a minimum of $\tilde{v}_{90} = 0.920$ near $e = 0.25$, and a maximum of $\tilde{v}_{90} = 0.955$ near $e = 0.75$. When

averaging over a realistic smooth distribution $f(e)$, we get a robust prediction that $\tilde{v}_{90} \simeq 0.94 \pm 0.01$ for pure binaries in Newtonian gravity, with minimal dependence on the uncertain $f(e)$.

In Figure 7 we show the predicted distribution of \tilde{v} for 5 different distributions $f(e)$: the flat distribution $f(e) = 1$; the distribution $f(e) = 0.4 + 1.2e$ fitted from Tokovinin & Kiyaveva (2016); and three power-law models $f(e) = (1 + \gamma)e^\gamma$ with $\gamma = 0.5, 1, 1.3$. The $\gamma = 1$ model is equivalent to the “thermal” distribution $f(e) = 2e$, while $\gamma = 1.3$ is close to the super-thermal distribution favoured by Hwang et al. (2022). In this Figure 7, we see that the flat $f(e)$ produces a pointed peak, resulting from the caustic spike from low- e orbits. As the distribution is weighted more to higher e , the \tilde{v} histograms become more rounded, the mean and mode shift to lower values, but the skewness increases and the upper tail grows slightly. The Tokovinin and $\gamma = 0.5$ models, though different, produce very similar \tilde{v} distributions. There is a pivot point where all models nearly intersect near $\tilde{v} \simeq 1$, so the total fraction above $\tilde{v} \geq 0.9$ is nearly constant: this fraction is between 12.6 and 12.8 percent for all five $f(e)$ distributions above.

Later it is also useful to consider the fraction of pure binaries giving $\tilde{v} \geq 0.8$: this is slightly more sensitive to the $f(e)$ distribution, but offers a larger percentage for improved statistics, and a larger ratio of binaries to triples in the modelling, hence is less sensitive to details of the triple modelling. For fixed e this fraction at $\tilde{v} \geq 0.8$ monotonically declines from 29.2 percent at $e = 0$ to 16.8 percent at $e = 0.95$; however, when averaging over a reasonable $f(e)$ distribution this variation is substantially reduced, giving 23.2 percent for flat $f(e)$, 21.9 percent for both Tokovinin and $\gamma = 0.5$ models, 21.0 percent for $f(e) = 2e$, and 20.6 percent for the $\gamma = 1.3$ model.

In our example MOND model (see below), though numerical orbits are not closed, each single orbit at separation $\gtrsim 10 \text{ kAU}$ is roughly approximated by a Keplerian orbit with an effective G boosted by a factor 1.36, and velocities boosted by a factor 1.17; our definition of \tilde{v} has the Newtonian v_c on the denominator, thus the predicted \tilde{v} distribution in MOND is very similar to the Newtonian prediction rescaled by this factor of 1.17 multiplicative shift.

As a result of this, the MOND models produce a dramatic increase in fractions of binaries above \tilde{v} thresholds of 0.8 or 0.9: the MOND model with $f(e) = 2e$, for binaries wider than $r_p \geq 10 \text{ kAU}$, predicts 33.7 percent at $\tilde{v} \geq 0.8$ and 24.4 percent above $\tilde{v} \geq 0.9$. These are substantially larger fractions compared to Newtonian predictions above, which **cannot be reproduced in a Newtonian model with any eccentricity distribution**. Therefore, if we had a sample of $\gtrsim 1000$ “pure” wide binaries, we could readily distinguish between Newtonian gravity and MOND by simply testing whether \tilde{v}_{90} is near 0.94 or 1.10, or testing whether the fraction above $\tilde{v} > 0.9$ is near 12 percent vs 24 percent; these would be easily distinguishable at high significance.

However, we do not currently have a sample of “pure” binaries: the observed distribution of \tilde{v} shows an extended tail up to much larger values $\tilde{v} \gtrsim 4$, as originally noted by PS19 in *Gaia* DR2 data, and confirmed in PS23. Although MOND does allow bound binaries with \tilde{v} values

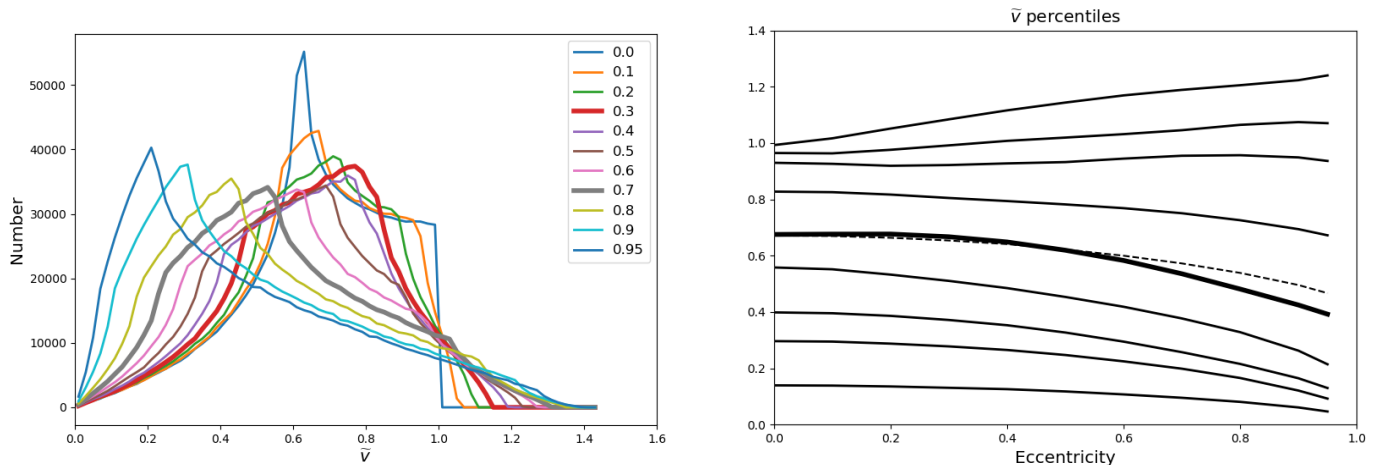


FIG. 6.— Left panel: Probability distribution of \tilde{v} for simulated binary orbits with fixed values of e , from 0.0 to 0.9 in steps of 0.1, also 0.95. Values are as labelled in the legend; $e = 0.3$ and 0.7 are thicker lines. Right panel: Selected percentiles of \tilde{v} distribution for orbits with fixed e (abscissa). Solid lines are percentiles 1 (bottom), 5, 10, 25, 50 (thick line), 75, 90, 95, 99 (top). The dashed line is the mean.

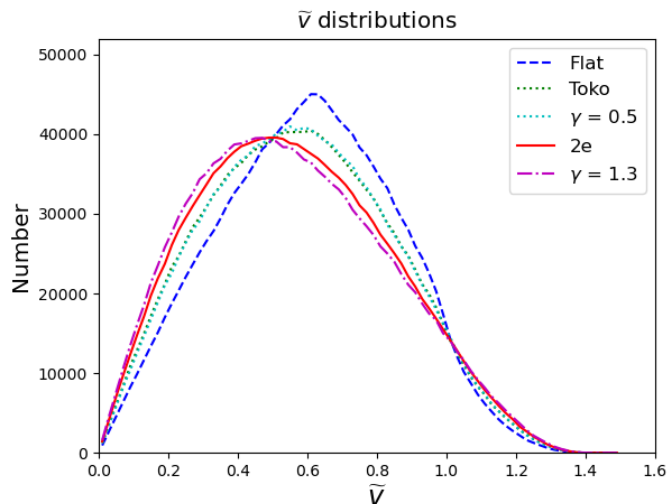


FIG. 7.— Probability distribution of \tilde{v} for five eccentricity distributions $f(e)$: flat $f(e) = 1$ (dashed, blue); model $f(e) = 0.4 + 1.2e$ from Tokovinin & Kiyayeva (2016) (dotted, green); power-law model with $\gamma = 0.5$ (dotted, cyan); thermal distribution $f(e) = 2e$ (solid red); and power-law model with $\gamma = 1.3$ from Hwang et al. (2022) (dot-dash, magenta). Note that the $\gamma = 0.5$ and Tokovinin models give a very similar result.

above the Newtonian limit of $\sqrt{2}$, values above $\tilde{v} \geq 1.75$ cannot be achieved in a reasonable MOND model with external field effect, and values above 1.5 are very rare in our MOND simulations (frequency ~ 0.1 percent); thus this extended tail is almost certainly not pure binaries, but is dominated by triple, higher-order or unbound systems. In Section 4 later, we fit the observed \tilde{v} distributions as a mixture of simulated binary, triple and unbound systems in both Newtonian and MOND gravity, with the \tilde{v} distributions for model systems generated as described in the following subsections, then relative abundances allowed to vary in the fitting in Section 4.

3.2. Binary orbit simulations

Similar to Section 3 from PS23, here we simulate a large sample of $\sim 5 \times 10^6$ orbits in both Newtonian

gravity and a specific modified-gravity model; as before we use the model from Banik & Zhao (2018) (hereafter BZ18).

For the MOND models, the orbits are not closed and not strictly defined by the standard Keplerian parameters a , e . As in PS23, we parametrise using the “effective” orbit size \hat{a} and quasi-eccentricity \hat{e} as follows: we define \hat{a} to be the separation at which the simulated relative velocity is equal to the circular-orbit velocity (in the current modified-gravity model), then we define θ_{circ} to be the angle between the relative velocity vector and the tangential direction when the orbital separation crosses \hat{a} , and then $\hat{e} \equiv \sin \theta_{\text{circ}}$; these definitions coincide with the usual Keplerian a , e in the case of standard gravity.

In both gravity cases, we simulate orbits with a distribution function $^1 dn/d\hat{a} \propto \hat{a}^{-1.6}$ for \hat{a} between $0.3 \text{ kAU} \leq \hat{a} \leq 150 \text{ kAU}$ (much wider than the data sample to avoid edge effects); this -1.6 power law is consistent with observations, e.g. Lépine & Bongiorno (2007), Andrews et al. (2017), El-Badry & Rix (2018). We use a $\gamma = 1.3$ distribution for \hat{e} .

The only modified-gravity model we consider below is the MOND model with ExFE, using the approximation of BZ18; this is given by

$$g_{N,int} = G(M_1 + M_2)/r^2 \quad (8)$$

$$g_{N,gal} = 1.2 a_0 \quad (9)$$

$$g_{N,tot} = (g_{N,int}^2 + g_{N,gal}^2)^{1/2} \quad (10)$$

$$g_{i,EF E} = g_{N,int} \nu(g_{N,tot}/a_0) \left(1 + \frac{\kappa(g_{N,tot})}{3} \right) \quad (11)$$

$$\kappa \equiv \frac{\partial \ln \nu}{\partial \ln g_N} \quad (12)$$

where $g_{N,int}$ is the internal Newtonian acceleration of the binary; $g_{N,gal}$ is the external (Galactic) Newtonian acceleration, $g_{N,tot}$ is the quadrature sum of these, ν is the MOND ν function defined in McGaugh et al.

¹ This turns out to be the most significant change from v1 of this paper; see discussion later in Sec 4.4.

(2016) which produces a good fit to spiral galaxy rotation curves, which is

$$\nu(y) = \frac{1}{1 - \exp(-\sqrt{y})}, \quad (13)$$

and $g_{i,EFE}$ is our model MOND-ian internal acceleration, approximating the application of the external field effect. (This is not quite an exact solution of the MOND-like equations, but is shown by BZ18 to be a good approximation to the full numerical solution).

3.2.1. Model perspective effects

We also model perspective effects on the velocity differences, as in Eq. 6 of PS18, multiplied below by d to convert proper motion to velocity units. Perspective effects are modelled as follows: for each simulated observation, we model the barycenter velocity as an isotropic Gaussian with a velocity dispersion of 25 km s^{-1} in each coordinate. Given the simulated distance and random viewer direction, we calculate the barycenter radial velocity v_r , transverse velocity v_{tan} , and radial separation Δd and angular separation θ . We then add a term $\Delta v_{shrink} = -v_r \theta$ (for θ in radians) parallel to the angular separation direction for the apparent contraction of the binary due to its radial velocity, and another term $\Delta v_{ov} = v_{tan}(\Delta d/d)$ for the closer component apparently overtaking the more distant one in the direction parallel to \mathbf{v}_{tan} ; these are added as vectors to the simulated orbital velocity difference $\Delta \mathbf{v}_P$ before converting to \tilde{v} . These perspective terms turn out to make only a minor change to the overall results; the effect can become significant for wide separations $r_p \gtrsim 10 \text{ kAU}$ and small distances $\lesssim 100 \text{ pc}$, but these systems are a small fraction of our total sample.

3.2.2. Model proper motion errors

In the binary-orbit simulations, we add simulated measurement noise to the theoretical \tilde{v} values as follows: we use simulated G magnitudes for both stars input to the fitting formula of Klüter et al. (2020) for the rms position error per single *Gaia* scan,

$$\sigma_{AL} = \frac{100 + 7.75 u}{\sqrt{9}} \text{ microarcsec} \quad (14)$$

$$u \equiv \sqrt{-1.631 + 680.766 z + 32.732 z^2}$$

$$z \equiv 10^{0.4[\max(G,14)-15]}$$

where σ_{AL} is the 1D along-scan astrometric precision for a single focal plane transit, crossing 9 CCDs.

Evaluating Eq. 14 vs magnitude, then comparing with the median proper motion errors vs magnitude from Table 4 of Lindegren et al. (2021), we find by inspection that rescaling σ_{AL} by a multiplier of $0.26/\text{year}$ produces a good approximation to the median observed proper motion errors in that Table: so we adopt model proper motion errors of $0.26 \sigma_{AL} \text{ yr}^{-1}$ per coordinate for each star, using its simulated magnitude in Eq. 14. These values for both simulated stars are added in quadrature, and multiplied by distance then divided by circular-orbit velocity to give an equivalent scatter in \tilde{v} . We generate independent Gaussians for the error components parallel and perpendicular to the error-free \tilde{v} , and take the mag-

nitude of the resultant 2D vector as the simulated noisy \tilde{v} .

3.3. Triple system simulations

To simulate a population of triple systems, we generate two binary orbits made up of three stars. We choose labels so star 1 is the single star in the wide system, and stars 2 & 3 comprise the inner binary, so the outer orbit is star 1 orbiting the barycentre of stars 2 and 3. For the masses, for stars 1 and 2 we pick masses from a Kroupa et al. (2013) IMF distribution, which is then multiplied by $(M/0.95 M_\odot)^{-2.5}$ for $M > 0.95 M_\odot$ to give a present-day main-sequence mass function assuming constant past star-formation rate. We then pick a random distance with distribution $\propto d^2$ within 300 pc; we then compute simulated apparent G magnitudes, if both are $G < 17$ we accept the pair, otherwise discard and re-select. Star 3 is then assigned $M_3 = q M_2$ with q uniform in the range $[0.02, 1]$.

For orbit sizes, we choose the outer orbit size \hat{a}_{out} with a power-law distribution $p(\hat{a}_{out}) \propto \hat{a}_{out}^{-1.6}$ within the range $0.3 \text{ kAU} \leq \hat{a}_{out} \leq 150 \text{ kAU}$, as for the pure binaries above; and the inner orbit size a_{inn} is chosen from the lognormal distribution given by Offner et al. (2023) for FGK stars; this is a lognormal where $\log_{10} a_{inn}$ is a Gaussian with mean $\log_{10}(40 \text{ AU})$ and standard deviation 1.5; we also apply an upper limit to a_{inn} for stability, based on the fitting formula of Tokovinin (2014) as

$$\frac{a_{inn}}{\hat{a}_{out}} \leq \max(0.342(1 - \hat{e}_{out})^2, 0.01) \quad (15)$$

For eccentricities, our default model uses the power-law distribution of Hwang et al. (2022) which is $f(e) = (1/2.3)e^{1.3}$ for the outer orbit; and the linear model from Tokovinin & Kiyaveva (2016), which is $f(e) = 0.4 + 1.2e$ for the inner orbit; inner and outer eccentricities are uncorrelated from these distributions.

For simplicity, we treat the inner and outer orbits as independent. We solve for the two orbits independently in their own planes, and then apply a random 3D rotation matrix, \mathbf{R} , to the inner orbit relative velocity to generate a random relative alignment between the two orbits. Next the system is “observed” at ~ 10 random phases and 5 random viewing directions for each phase. At each simulated “observation” we evaluate the projected separation, and the 3D velocity difference between star 1 and the “observable center” of stars 2+3, as follows.

$$\mathbf{v}_{3D,obs} = \mathbf{v}_{out} - f_{pb} \mathbf{R} \mathbf{v}_{inn} \quad (16)$$

where \mathbf{v}_{out} is the outer orbit velocity (star 1 relative to the barycentre of 2+3), and \mathbf{v}_{inn} is the relative velocity between stars 2+3. In a refinement of PS23, instead of calculating the instantaneous velocity difference for \mathbf{v}_{inn} , we take the vector position difference at two epochs separated by 34 months, and divide this vector by 34 months, to obtain the time-averaged velocity over the baseline of the *Gaia* DR3 data; this accounts approximately for orbit-wrapping for short-period orbits.

This velocity \mathbf{v}_{inn} is rotated and scaled down by a dimensionless factor $f_{pb} \leq 0.5$, defined as the fractional offset between the “observable centre” and the barycentre of stars 2+3, relative to their actual separation. The

“observable centre” is defined according to the angular separation: if less than 1 arcsec, we assume stars 2+3 are detected by *Gaia* as a single unresolved object, and use the luminosity-weighted centroid (photocentre) of the two. Otherwise for separation > 1 arcsec, we assume stars 2 and 3 are detected as separate objects, or star 3 is unobservably faint, and we take the position of star 2 alone as the observable centre. Therefore, this results in a fractional offset given by

$$f_{pb} = \begin{cases} \frac{M_3}{M_2+M_3} - \frac{L_3}{L_2+L_3} & (\theta < 1 \text{ arcsec}) \\ \frac{M_3}{M_2+M_3} & (\theta \geq 1 \text{ arcsec}) \end{cases} \quad (17)$$

where the $L_{2,3}$ are the model luminosities.

The 3D resultant velocity Eq. 16 above is then converted to 2D projected velocity according to each random viewing direction, and observables including r_p, \tilde{v} are saved to create simulated histograms for triple systems; this procedure is repeated for both of the gravity models (Newtonian and MOND).

We also include the “apparent mass” bias for triples: the actual outer-orbit velocity depends on the sum of all three masses, while in calculating \tilde{v} the mass of star 2 is estimated from the combined luminosity $L_2 + L_3$; this $M_{2,est}$ is smaller than the true $M_2 + M_3$, so the calculated \tilde{v} is boosted by a multiplicative factor of $\sqrt{[(M_1 + M_2 + M_3)/(M_1 + M_{2,est})]}$, compared to the value using the unknown true mass sum.

3.3.1. Simulating the triple cuts

For a realistic triple simulation, we also need to include the effect of the cuts on **ruwe**, faint companions, **ipd_frac_multi_peak** and the Lobster diagram applied to our data sample above. These cuts selectively remove certain regions of triple parameter space, depending on the separation and mass ratio of the inner binary, so surviving triples have a somewhat different distribution of \tilde{v} to the original population. The **ruwe** cut preferentially removes triples with inner-orbit period in a broad window around 3 years, while it is insensitive to very small or very large orbits. The **ipd_frac_multi_peak** cut preferentially removes inner angular separations $\gtrsim 0.3$ arcsec, while the Lobster cut removes inner pairs with roughly similar luminosities, independent of separation.

For the **ruwe** cut, we simulate a **ruwe** value for the inner orbit: the simulated G magnitude of star 2 is used as input to the fitting formula of Klüter et al. (2020), Eq. 14 above. We then approximate the rms dispersion of the photocentre of stars 2 + 3 from the barycentre over a full orbit as

$$\sigma_{cen} \equiv f_{pb} a_{inn}/(2d) \quad (18)$$

where the factor of 2 accounts for $1/\sqrt{2}$ for *Gaia*’s 1D scanning and a second $1/\sqrt{2}$ approximates projection factors; we then adapt the fitting formula from Penoyre et al. (2022) and define the simulated **ruwe** value as

$$\text{ruwe}_{sim} \equiv \frac{\sqrt{n_{orb}^4 \sigma_{cen}^2 + \sigma_{AL}^2}}{\sigma_{AL}} \quad (19)$$

$$n_{orb} \equiv \min(1, T/P_{inn}) \quad (20)$$

where the n_{orb} factor accounts for the suppression of the residuals for long-period orbits with $P_{inn} \geq T$ where only

a partial arc is observed, and the linear term is absorbed into the *Gaia* proper motion fit. We then reject simulated systems with $\text{ruwe}_{sim} > 1.2$.

For the **ipd_frac_multi_peak** cut, we simulate this by rejecting triples where the inner binary has angular separation > 0.3 arcsec and magnitude difference < 4 mag.

For the Lobster cut, we reject simulated triples when the inner binary is more than 0.4 mag above the main sequence ridge-line, which corresponds to a mass ratio $M_3/M_2 > 0.8$.

The combined cuts above reject 61.3 percent of our simulated triple systems, leaving 38.7 percent surviving all the cuts. The **ruwe** cut is the most effective, rejecting 42% of the original sample; the Lobster cut rejects a further 11 %; while the **ipd_frac_multi_peak** cut and faint-companion cuts together reject 8 %. Figure 8 shows the distribution of \tilde{v} for triples pre- and post-cuts, and with proper motion errors added as in Section 3.2.2 above. The survival fraction is a gently rising function of \tilde{v} , from $\approx 34\%$ at small \tilde{v} to $\approx 46\%$ at large \tilde{v} . The survival fraction is weakly dependent on r_p , as expected since the cuts depend on inner-orbit parameters, not outer-orbit values. The effect of proper motion errors is nearly negligible here, as the intrinsic width of the triple distribution is much broader than the errors.

Some selected summary statistics of the \tilde{v} distribution for triples are listed in Table 2; these may be useful for comparison with future work with data or other triple models. These simulated triple distributions in the r_p, \tilde{v} plane are then used (with fixed shape and variable normalisation) in the fitting procedure below in Section 4.

Histograms of \tilde{v} for triples in some selected outer-orbit r_p bins are shown in Figure 8, and selected summary statistics for each r_p bin are listed in Table 2. The triple histograms show a peak around $\tilde{v} \sim 0.7 - 0.9$, increasing slightly with r_p ; this peak is only moderately shifted from the location $\tilde{v} \approx 0.55$ for pure binaries; the relatively modest shift is due to common cases where the inner binary produces only a small velocity perturbation, due to orbit-averaging for short periods, and/or small f_{pb} for mass ratios near 0 or 1. Unlike binaries, the triple distributions show a long tail extending well beyond $\tilde{v} \sim 2$; the tail becomes more extended at larger r_p , due to the effective $\sqrt{r_p}$ factor in \tilde{v} .

The length of the tail can be approximately explained because two effects above produce an effective ceiling on the magnitude of $f_{pb} \mathbf{v}_{inn}$: considering for simplicity fixed masses, a circular orbit and varying period P , the change of separation vector \mathbf{r}_{23} over a time baseline T is $\Delta \mathbf{r}_{23} \propto P^{2/3} \sin(\pi T/P)$. The global maximum of this occurs for $P = \pi T/u$ where $u = 0.9674$ is the smallest positive solution of $\tan u = 3u/2$, giving $P \simeq 3.25 T$. Taking an example inner binary of $0.8 + 0.4 M_\odot$ and $T = 34$ months for DR3, this gives a maximum time-average velocity $\Delta \mathbf{r}_{23}/T$ of 12.8 km s^{-1} . Also, the maximum of f_{pb} for an unresolved system is $\simeq 0.25$ so the maximum of $f_{pb} \mathbf{v}_{inn}$ is then $\sim 3.2 \text{ km s}^{-1}$. Larger masses and non-circular orbits will allow slightly higher values, but there is also a reduction by sky projection, so overall the velocity effect of inner binaries is much smaller than we may expect from the familiar 29.8 km s^{-1} for a $1 M_\odot$ binary at 1 AU circular orbit. There is indeed a notable decline in density in Figure 3 above $\Delta v_p \sim 3 \text{ km s}^{-1}$; This

Triple model comparison

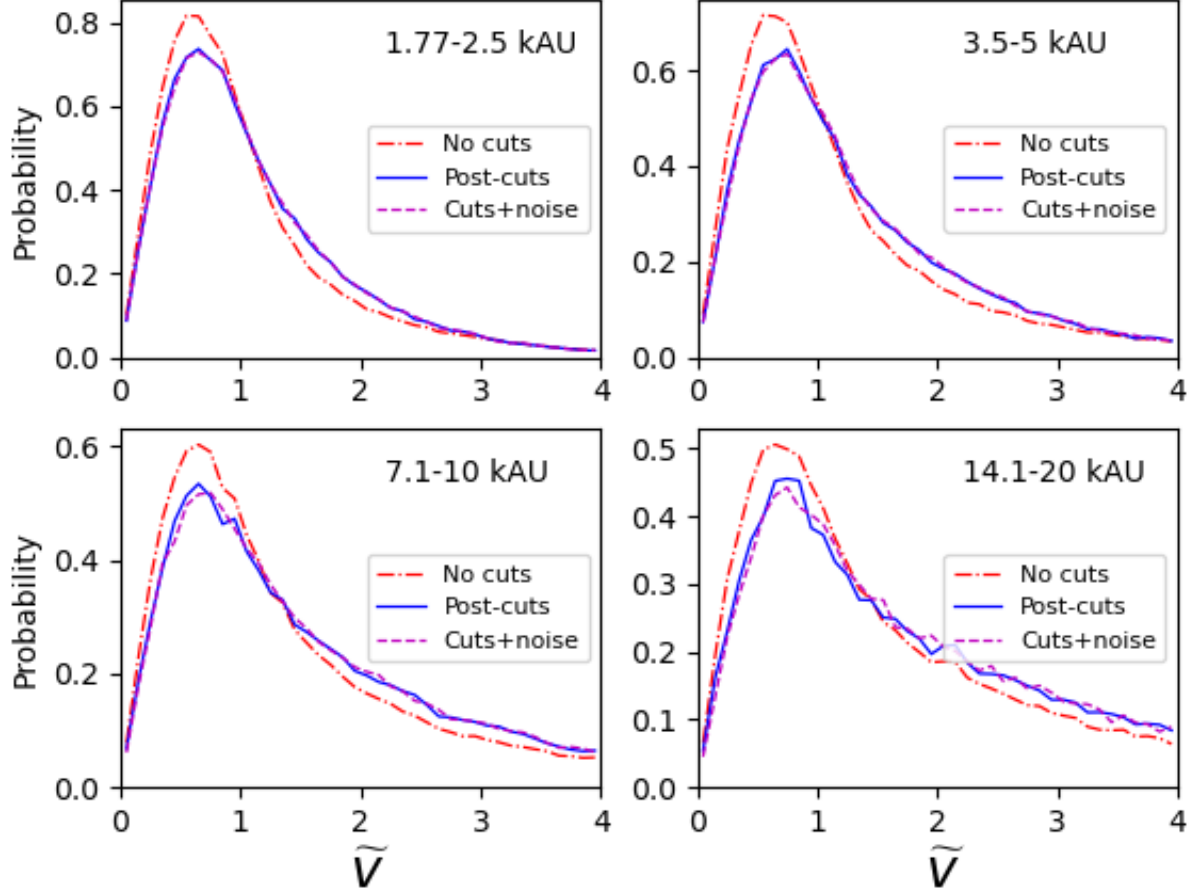


FIG. 8.— Histograms of \tilde{v} for our baseline triple simulation, in 4 selected bins of outer orbit r_p as labelled in the legend. (Every second r_p bin is shown for brevity). Red dot-dashed line: before cuts. Blue/solid line: after cuts, noise-free, renormalised to unit area. Magenta dashed line: after cuts with simulated \tilde{v} noise.

TABLE 2

SUMMARY STATISTICS OF \tilde{v} FOR THE BASELINE TRIPLE MODEL, AFTER SIMULATED CUTS, IN BINS OF PROJECTED SEPARATION r_p . COLUMNS 2–4 ARE PERCENTAGES OF TRIPLE SYSTEMS (IN THIS r_p BIN) IN SELECTED \tilde{v} RANGES; COLUMNS 5–6 ARE MEDIAN AND 90TH PERCENTILE OF \tilde{v} .

r_p bin (kAU)	Percentage in \tilde{v} range:			Percentiles of \tilde{v} :	
	$\tilde{v} < 0.8$	$\tilde{v} \in (0.8, 1.5)$	$\tilde{v} > 1.5$	Median	90th percentile
1.25 – 1.77	44.6	35.3	20.0	0.87	1.98
1.77 – 2.5	41.5	33.9	24.6	0.93	2.24
2.5 – 3.5	37.9	33.1	29.0	1.00	2.51
3.5 – 5.0	34.9	31.2	34.0	1.08	2.88
5.0 – 7.1	32.5	28.7	38.8	1.17	3.34
7.1 – 10.0	29.2	26.5	44.2	1.31	3.85
10.0 – 14.1	26.2	24.9	48.9	1.46	4.42
14.1 – 20.0	23.1	23.0	53.9	1.66	5.16

corresponds to $\tilde{v} \sim 3$ for a 1 kAU outer orbit, or $\tilde{v} \sim 10$ for a 10 kAU outer orbit. So, the tail of triples to large \tilde{v} is bounded as observed in Figure 8, but this bound increases $\propto \sqrt{r_p}$. This also suggests that our original selection cut of $\Delta v_p \leq 5 \text{ km s}^{-1}$ above is wide enough to include almost all bound binary and triple systems at $r_p \geq 1.25 \text{ kAU}$; none of our simulated triple systems at $r_p \geq 1.25 \text{ kAU}$ exceeded $\Delta v_p > 5 \text{ km s}^{-1}$.

3.4. Random Samples

As a refinement of Pittordis & Sutherland (2023), we also include in the fitting a population of “random” associations: this population was generated in PS23 by randomising single star positions by a few degrees (keeping other parameters unchanged) then re-running the binary search, and repeating 9 times. Since the number of randoms per bin is relatively small, the statistical uncertainties per bin are rather large. Therefore, we simply create a smooth population of randoms normalised to the mean total per simulation. Since the Galactic rms velocity dispersion is considerably larger than the 5 km s^{-1} maximum velocity difference considered here, phase-space considerations show that the expected population of randoms follows a distribution function given by $dN_r \propto v_p r_p dv_p dr_p$. Changing variables from v_p to \tilde{v} leads to $dN_r \propto \tilde{v} d\tilde{v} dr_p$. We adopt this distribution scaled to match the measured mean number of randoms per run with $\tilde{v} \leq 7$ in the outer bin $14.1 < r_p < 20 \text{ kAU}$, which is 37.

It will be seen below that the randoms make a very small contribution to the final fits, except in the outermost 2 bins.

3.5. Flyby simulations

Similar to PS23, we simulate a population of unbound low-velocity “flyby” systems; this is assumed to result from unbound pairs which have very similar 3D velocities due to having been born in the same open cluster but escaped independently; this means that they retain a “memory” of their initial orbits and have velocity differences much smaller than random unassociated pairs. An alternative source of such systems is given by Jiang & Tremaine (2010), who modelled evolution of wide-binary systems under random encounters with other stars and the Galactic tidal field; they found that binaries wider than $\sim 20 \text{ kAU}$ have a substantial probability of becoming unbound within the age of the Galaxy, but can remain within separations of a few pc for a long time after unbinding, and occasionally approach closer.

We simulate these as hyperbolic orbits with asymptotic velocities v_∞ uniform and random from 0 to 2 km s^{-1} , and model a realistic distribution of impact parameters; we take random snapshots of these orbits, discard systems with 3D separations above 200 kAU and “observe” the surviving pairs from random viewing directions. Note that in 3D space, these hyperbolic systems must have $\tilde{v}_{3D} > \sqrt{2}$, but in 2D the projection factors fill in the hole at $\tilde{v} < \sqrt{2}$ giving a smooth distribution. It turns out that the shape of the \tilde{v} distribution for any single r_p bin is not very different from the triples, however the flyby population increases steeply with r_p , while the triple population decreases with r_p roughly in proportion to the binaries; see below for implications for the fitting.

4. DATA VS MODEL FITTING

In this section we fit the observed distributions of \tilde{v} in our DR3 wide-binary sample as a mixture of binary, triple, flyby and random systems, where the shape of the \tilde{v} distribution for each population is fixed by the results of the simulations in Section 3, while the relative normalisations of each population are adjusted to fit the data. We repeat this for both Newtonian and MOND gravity models, and several eccentricity distributions.

We take the bins as defined above in projected separation spanning 1.25 kAU to 20 kAU in total; this range is split into 8 logarithmic bins with each bin upper edge $\sqrt{2} \times$ the lower edge, so the first bin spans 1.25 to 1.77 kAU and the eighth bin is 14.1 to 20 kAU; this places the first two bins in the quasi-Newtonian regime where MOND effects should be small, bins 3 – 5 are in a transition regime, while the final three bins are well into the MOND regime with internal accelerations $\lesssim a_0$. We then fit simultaneously to all eight observed \tilde{v} histograms, using 9, 10 or 11 adjustable parameters: below we first describe our “baseline” 10-parameter model fit in some detail in the next subsection, then explore some variations in the base fits in the subsequent subsection.

4.1. Base model fits

Our base model uses 10 adjustable parameters for normalization of the model distributions: the first 8 parameters $n_{bt,j}$ for $1 \leq j \leq 8$ are simply the total number of model binary+triple systems in the j th bin, the 9th parameter f_{trip} is the fraction of triples among (binaries + triples), kept equal across all bins; and the 10th parameter n_{fly} is one overall normalisation for the flyby population (with the relative numbers per bin fixed as in the simulation). The random population is included in the model fitted, but fixed as in the previous section. Then, for each bin the model populations are normalised such that the bin j contains $(1 - f_{\text{trip}}) n_{bt,j}$ binaries, $f_{\text{trip}} n_{bt,j}$ triples, the flyby model is renormalised so there are n_{fly} flybys in the 7 – 10 kAU bin (this bin arbitrarily defined), and all other bins are rescaled by the same factor so relative number of flybys per bin remains the same as the simulation; and the model randoms are fixed as above with pre-defined normalisation. These four populations are then added to give a total model \tilde{v} histogram for each of the 8 bins. (Note that the use of a single normalisation parameter for the flyby population across all bins is helpful here: in our previous paper PS23, the four r_p bins were fitted independently which led to a substantial degeneracy between flyby and triple populations. With the simultaneous fit as here, the r_p distribution of the flybys is fixed, which breaks this degeneracy.)

We then fit a maximum-log-likelihood fit to the observed histograms of \tilde{v} , varying these 10 parameters to maximise the summed log-likelihood of all 8 bins combined, using the Python `lmfit` fit package and a Nelder-Mead simplex search; log-likelihoods are calculated using the data and Poisson statistics from the total model distribution as above (this is formally better than a χ^2 minimisation, due to small-number statistics in the tails at high \tilde{v}).

We then run the fit as above for both the Newtonian and MOND binary+triple orbit models: flyby and random models are in common, but all the parameters are

independent between the two fits. The results of our baseline fits are shown for the Newtonian model in Figure 9, for MOND in Figure 10, and best-fit parameters listed in Table 3.

The most notable feature is that the best-fit Newtonian model produces a dramatically better χ^2 than the best-fit MOND model, respectively 424 for Newton vs 704 for MOND, i.e. a difference $\Delta\chi^2 = 280$ which is formally extremely significant. The expected χ^2 given the 8×40 histogram data values fitted is 310, so both fits are formally unacceptable; however the Newtonian model has a χ^2 per degree of freedom of 1.37 which is not unusual for real-world data. If we divide both χ^2 values by this factor, then the $\Delta\chi^2$ for MOND-Newton becomes 205 which is still very large; it appears that the Newtonian fit is preferred at very high significance.

On inspection of the Figures, both models produce a reasonable fit at small $\tilde{v} \lesssim 0.5$ and in the extended tail $\tilde{v} > 1.5$ which is triple-dominated; the main deviation of the MOND fits is that the MOND models systematically over-predict the data in the key region $0.8 \leq \tilde{v} \leq 1.2$, due to the predicted “rightward stretch” of the binary population predicted by MOND: this stretch therefore appears **not to be present** in the data. The Newtonian fits are much closer to the data in this key \tilde{v} region.

We show the individual χ^2 values per bin for both models in Figure 11; this shows that all the individual bins prefer Newtonian, with the strongest preference in the 3.5 – 5 kAU bin. This is slightly counter-intuitive because the MOND excess velocity grows with separation; however there are a larger number of systems in this bin, and the triple tail is less prominent, so this may well explain the result. The final two bins suffer somewhat from small-number statistics in the key region $0.8 \leq \tilde{v} \leq 1.4$.

Another point to note is that the $\Delta\chi^2$ (MOND-Newton) does decrease at small r_p , but does not reach zero. A probable reason is as follows: in our first bin $1.25 \leq r_p \leq 1.77$ kAU, model binaries have a median current 3D separation of 1.7 kAU, and the MOND effect at this separation is well below 1 percent excess over Newtonian, essentially negligible. However, the velocity depends on the MOND effect averaged over a full orbit; for this r_p bin 25% (10%) of the model binaries have an apocenter separation above 3.2 (5.2) kAU respectively, where the MOND effect reaches 4 (15) percent. Thus the orbit-averaged MOND effect is on average larger than the instantaneous value.

4.2. Variations on the base model

The results above appear highly significant, but with the caveat that they are limited to specific model shapes of the binary and triple populations and assumptions about unbound (flyby + random) populations. To check for sensitivity to various assumptions, we have explored a number of variations on the base model as follows:

Scale-dependent f_{trip} : Here we add an 11th free parameter, by allowing f_{trip} to be a linear function of $\log r_p$; specifically we use $f_{\text{trip}} = c_0 + c_1 j$ where j is the bin number, and fit for c_0, c_1 instead of f_{trip} . The result is the best-fit values are $c_0 = 0.173$, $c_1 = 0.0058$, so the variation in f_{trip} is relatively modest, with the 8th bin having $f_{\text{trip}} = 0.214$; the Newtonian χ^2 is 420, a reduction of only 4 from the base model, and the $\Delta\chi^2$ (MOND-

Newton) is 284.

Zero flybys, default randoms: Here we use a 9-parameter fit by fixing the flyby parameter n_{fly} to zero. The result is that f_{trip} increases to 0.193, the Newtonian χ^2 worsens to 443, and the $\Delta\chi^2$ (MOND-Newton) is 264.

Zero flybys, floating randoms: This is a 10-parameter fit with the flyby parameter n_{fly} again fixed to zero, but allowing the normalisation of the randoms to float. The Newtonian results give random normalisation 0.75, $f_{\text{trip}} = 0.195$ and $\chi^2 = 446$. The $\Delta\chi^2$ (MOND-Newton) is 264.

Double randoms: This is the same as the 10-parameter base fit except that the population of randoms is doubled from the default value. The result is that $f_{\text{trip}} = 0.182$, the Newtonian χ^2 is 435, and the $\Delta\chi^2$ (MOND-Newton) is 269

Base model, no perspective effects: This uses the same 10-parameter base fit, but the model binary and triple populations do not include perspective effects from Section 3.2.1. The result is $f_{\text{trip}} = 0.186$, the Newtonian χ^2 is 423, and the $\Delta\chi^2$ (MOND-Newton) is 273.

In summary, these variations on the base fit show that the preference for Newtonian gravity over MOND is not sensitive to variations in the random and flyby populations: the main feature of the fits is that the tail population at $\tilde{v} > 1.5$ is dominated by triples, with the randoms and flybys a minor contribution except in the widest r_p bin of 14.1 – 20 kAU. This property is well constrained, because the randoms and flybys cannot over-predict the tail in the latter bin; then their abundance falls off steeply in smaller bins due to their model r_p distributions, while the triples become more numerous towards smaller bins pro-rata with the binaries. This requires that the high \tilde{v} tail in most r_p bins is dominated by triples. Therefore, the observed amplitude of the tail constrains f_{trip} rather well. Given this, the models give a smooth extrapolation of the triples downwards below $\tilde{v} < 1$, so unless our triple model is for some reason substantially too high at $\tilde{v} \sim 1$, it seems hard to avoid the MOND models overshooting the data in this region.

4.3. Implications for triple fraction

The Newtonian fits above give a triple fraction of $f_{\text{trip}} = 0.185$ for the base model, with fairly small variations in the alternative fit models. The MOND model fits are systematically lower than this by ≈ 0.03 , in the direction expected due to the more extended underlying distributions in MOND.

Note that this f_{trip} is the fit *after* the simulated data-cuts are applied to the models. We can infer the fraction of triples pre-cut as follows. On average 38.7 percent of our simulated triples survive the data-cuts. The inferred pre-cut triple fraction is somewhat smaller than $0.185/0.387$ or 48 percent, since the denominator also includes triples. Assuming that nearly all pure binaries survive the data cuts, a population ratio of 18.5 triples to 81.5 binaries post-cuts would imply 48 triples per 81.5 binaries before the cuts, hence an original triple fraction of $48/(48 + 81.5)$ hence 37 percent; if the cuts reject a few binaries, this would be lowered slightly. This is significantly lower than the best-fit value $f_{CB} = 0.63$ in the nominal fit of Banik et al. (2024), and perhaps more realistic compared with observational estimates. We note

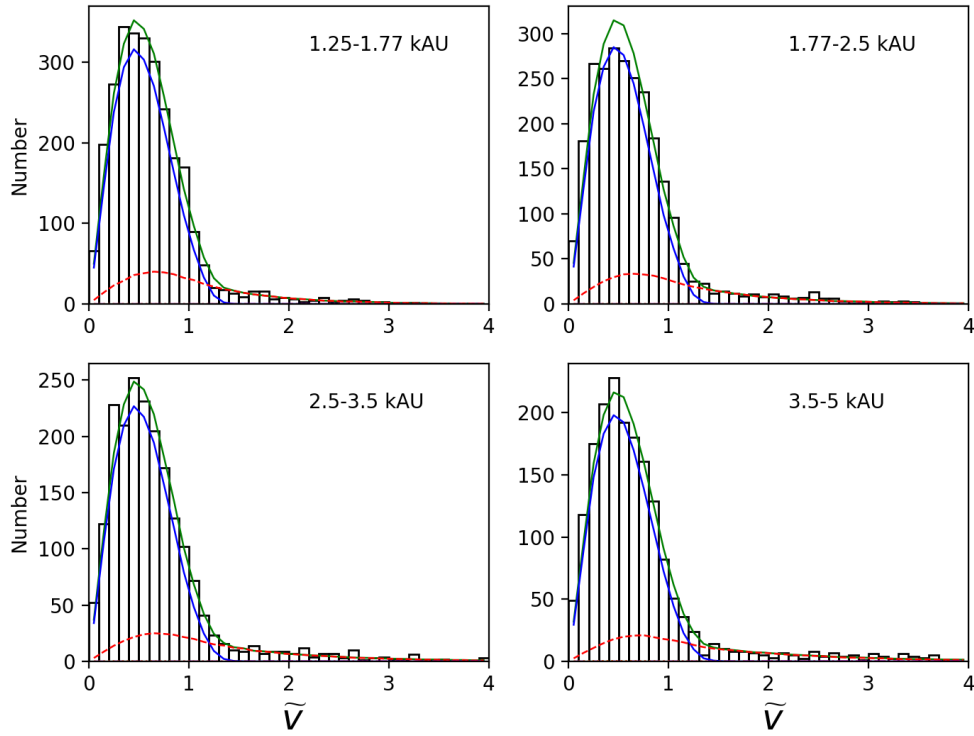
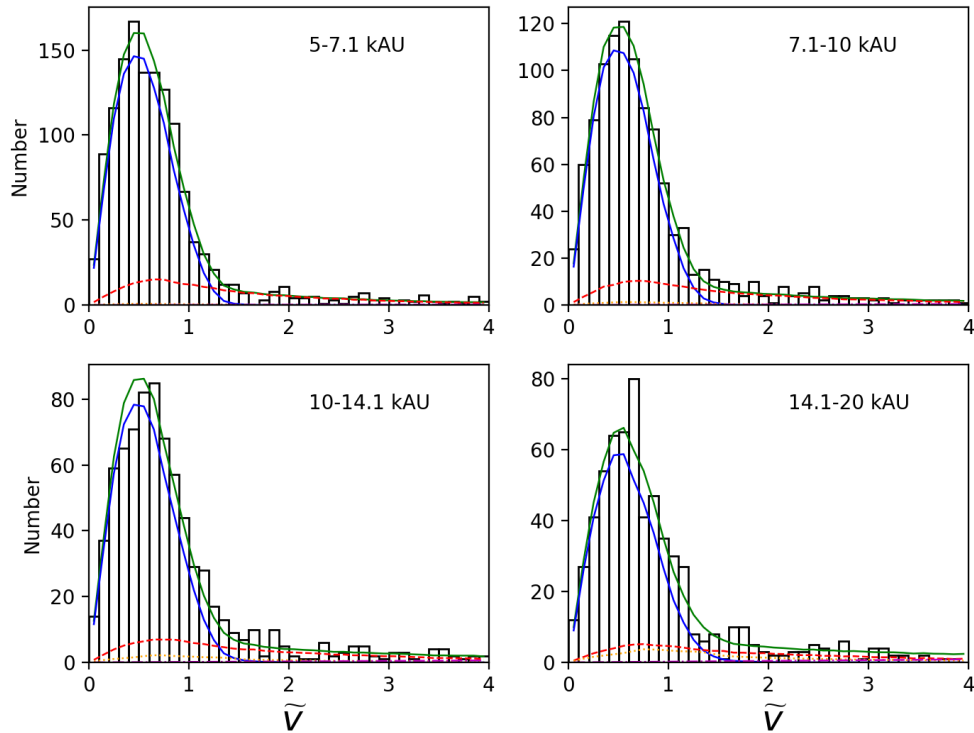
Fit: Newton, constant f_{trip} Fit: Newton, constant f_{trip} 

FIG. 9.— Fits of observed \tilde{v} histograms for the baseline Newtonian models. The 8 panels show different r_p bins as in the legend. Data is the black histogram. Lines show the total model fit (solid green, top), and subcomponents: binaries (solid blue, lower), triples (dashed red), flybys (dotted orange) and randoms (dot-dash magenta). The randoms are very low values except in the last two bins,

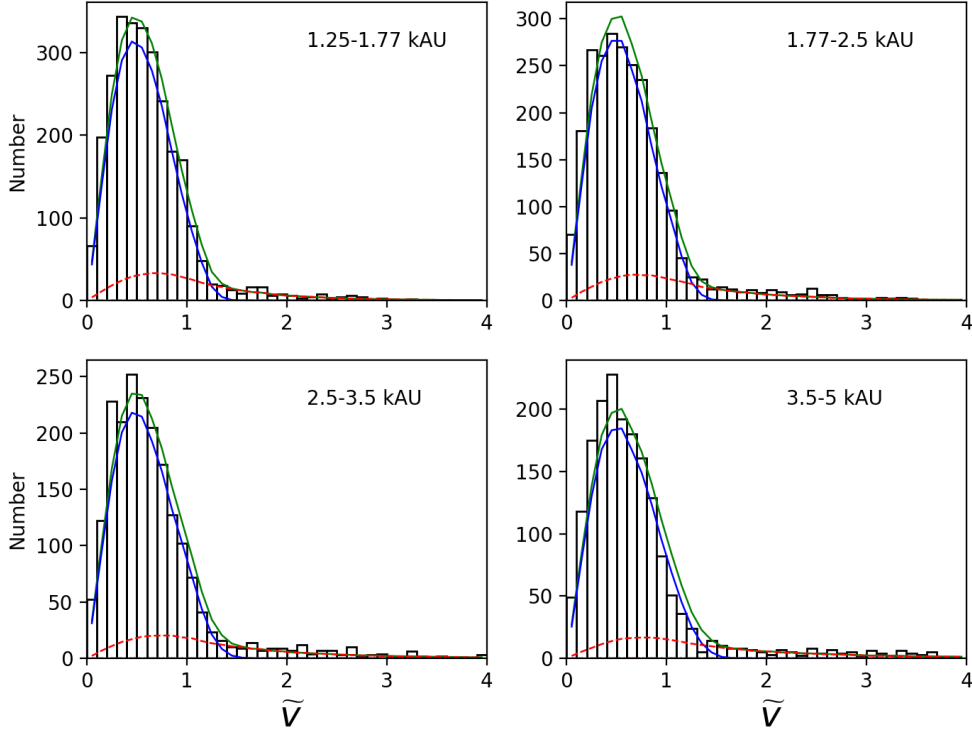
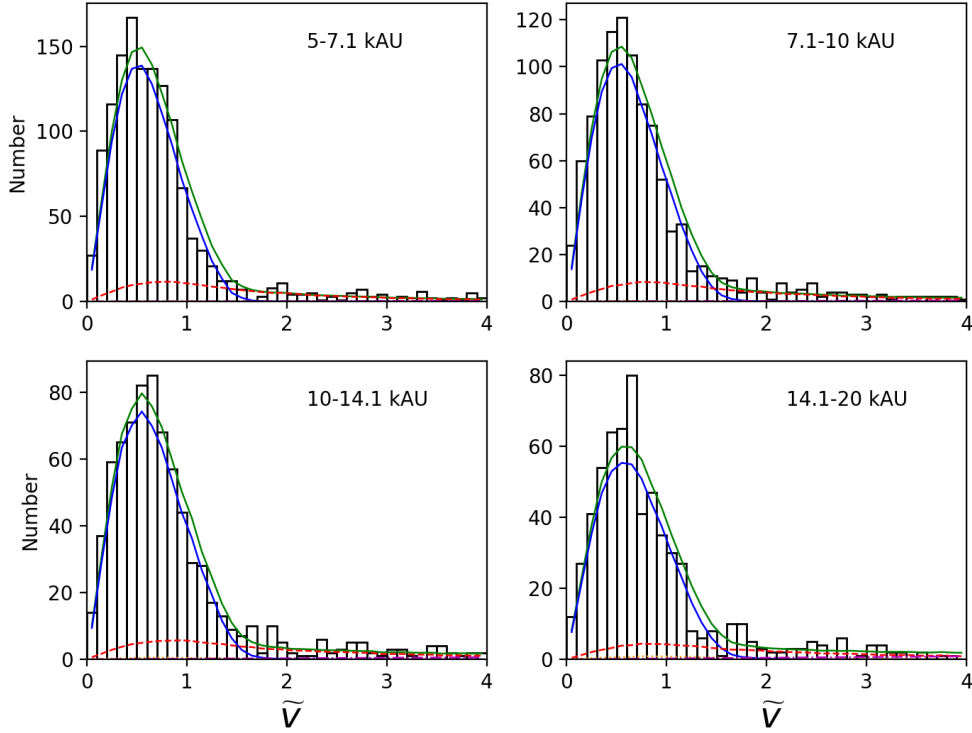
Fit: MOND, constant f_{trip} Fit: MOND, constant f_{trip} FIG. 10.— Same as Figure 9, but fitted with MOND model binary and triple \tilde{v} distributions.

TABLE 3
FIT PARAMETERS FOR BASELINE FIT, NEWTON AND MOND MODELS

r_p bin	Newton		MOND	
	$f_{\text{trip}} = 0.185$ n_{bt}	$n_{fly} = 17.9$ χ^2	$f_{\text{trip}} = 0.155$ n_{bt}	$n_{fly} = 4.1$ χ^2
1.25 – 1.77 kAU	2723	53.2	2724	77.1
1.77 – 2.5 kAU	2455	70.6	2456	104.6
2.5 – 3.5 kAU	1964	48.9	1966	97.1
3.5 – 5.0 kAU	1728	40.9	1731	112.3
5.0 – 7.1 kAU	1305	54.3	1312	103.0
7.1 – 10 kAU	990	36.9	1004	65.9
10 – 14.1 kAU	720	52.5	747	61.1
14.1 – 20 kAU	548	66.3	590	83.0

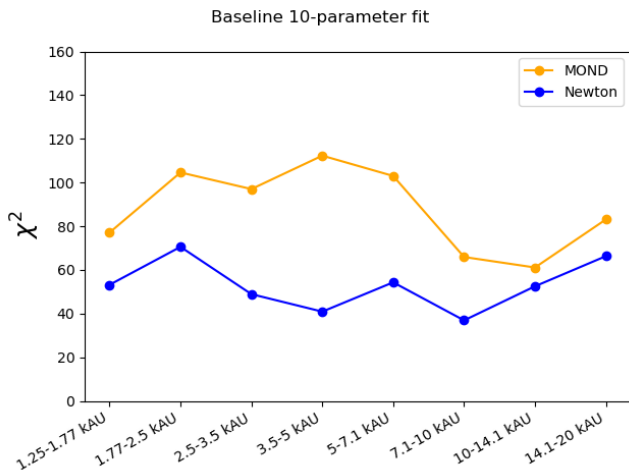


FIG. 11.— The fit χ^2 values, for the baseline fit, for individual r_p bins (x-axis) for Newtonian and MOND models

that Banik et al. (2024) also fitted the gravity model with f_{CB} constrained to a lower value of 0.30 (last row of their Table 3), and still found a strong preference for Newtonian gravity consistent with our results.

The 37 percent appears reasonable: e.g. in the WB formation model suggested by Kouwenhoven et al. (2010), wide-binaries form from capture of independently-born close systems during dissolution of an open cluster. A detailed study of multiplicity for solar-neighbourhood F/G dwarfs is given by Tokovinin (2014), with the result that systems with F/G primaries are 54% single, 33% binary, 8% triple, 4% quadruple, 1% higher order. Using the Kouwenhoven et al estimate that 15% of binaries are "wide" splits the binary contribution into 28% close binary, 5% wide binary, Assuming all the wide-binary systems originated from capture of two primordial single systems and that the remaining multiples are primordial, then the fraction of primordial single vs multiple systems would be $64/105 = 61\%$. We do not have comprehensive statistics for the lower-mass spectral types, K and early-M, which make up slightly over half our sample, but it is known that multiplicity is positively correlated with primary mass, so a primordial single fraction nearer 70% seems reasonable averaged over our mass distribution.

If we also assume that wide systems form from capture of two independent close systems, this would imply that wide systems are 49% pure binaries, and 51% triples or

higher-order multiples. This 51% of triples plus higher-order multiples is somewhat higher than our estimated 37%, but is not seriously discrepant.

4.4. Caveats and Limitations

The main limitations of our study is that we have only a single MOND model, and the parameter space of triple models is rather limited, though it is consistent with recent data from Offner et al. (2023) and Hwang et al. (2022). The related wide-binary study by Banik et al. (2024) used a more flexible parameter space of triple models, and reached the same preference for Newtonian over MOND gravity.

Another limitation is that we have not yet included quadruple (2+2) systems in our modelling; this is left for future work.

Here we have assumed that the estimated errors in *Gaia* proper motions are realistic, hence adding simulated magnitude-dependent errors to our modelled values. If the *Gaia* proper motion errors are systematically underestimated, or there is a strong non-Gaussian tail, this would tend to shift observed \tilde{v} values systematically upwards, with the relative effect increasing with r_p . This would tend to produce a false-positive MOND signal in the data, but this is in the opposite direction to our conclusion so is unlikely to be a serious problem.

In an earlier version of this paper, the $\Delta\chi^2$ values (MOND-Newton) were significantly higher at ~ 500 compared to ~ 280 above; both Newtonian and MOND χ^2 values are lower, but the MOND values lowered from ~ 1000 to 700 while Newtonian values lowered from ~ 500 to 420. The main reason for this shift is the change from a flat distribution in $\log a_{out}$ (i.e. $p(a_{out}) \propto a_{out}^{-1}$) to a steeper power-law $\propto a_{out}^{-1.6}$. We find that this shifts the pure-binary distributions of \tilde{v} by approximately a multiplicative shift of approx $0.96\times$. The reason is as follows: in 3D the \tilde{v}_{3D} in Newtonian gravity is simply $\sqrt{2-r/a}$; we observe in bins of r_p , while a is unknown. At a given r , systems have a range of a from $a \sim r/2$ to $a \gg r$. Those with $a > r$ have $\tilde{v}_{3D} > 1$ and those with $a < r$ have $\tilde{v}_{3D} < 1$. Changing to a more steeply declining a_{out} distribution leads to more of the latter and fewer of the former at a given r_p , hence the systematic shift. The 4% downward shift (in both Newtonian and MOND) is about 1/4 of the large-separation MOND effect, so the new MOND fits are less bad than previously.

4.5. Comparison with previous studies

Several earlier studies of wide binaries in *Gaia* EDR3/DR3 by Hernandez et al. (2022), Hernandez (2023), Hernandez et al. (2024b) Chae (2023), Chae (2024) have shown a strong preference for MOND over Newtonian gravity, thus directly opposite to our conclusion above; a review is given by Hernandez et al. (2024a).

Most of these analyses used fairly stringent cuts to remove triple systems, but then the surviving samples were analysed assuming zero residual contamination from triples. We argue here that this assumption is unlikely to be realistic, since triples with inner separations $\sim 5 - 50$ AU and dissimilar masses are not removable by any current cut: their orbit periods are too long to be rejected by a `ruwe` cut, their angular separations are too close to be resolvable, and mass ratios $q \lesssim 0.75$ will not be rejected by a Lobster-type cut; so systems like this will inevitably contaminate any present-day sample, at least until dedicated followup data is taken. Our modelling above indicates that 38.7 percent of our simulated triple systems survived all our cuts; this is clearly not a small fraction, therefore we believe that accounting for residual triples in the fit procedure is more realistic.

Residual triples have \tilde{v} values systematically larger than binaries, and for fixed inner orbits this shift increases with the outer orbit r_p due to the $1/\sqrt{r_p}$ term in the denominator of \tilde{v} ; so unaccounted residual triples tend to produce a MOND-like signal.

Chae (2024) does include model triples in the fits: however one issue is that his f_{trip} is normalised to match the median \tilde{v} in a small-separation bin, then held fixed in all other bins. This is questionable since the median \tilde{v} at small separations is not very sensitive to triples; another issue is that Chae’s sample is derived from El-Badry et al. (2021) and thus contains a cutoff $\Delta v_p \leq 2.1 \text{ km s}^{-1} (r_p/1 \text{ kAU})^{-0.5}$; converting to \tilde{v} gives $\tilde{v} \leq 2.24/\sqrt{M_{\text{tot}}}$. Therefore the extended tail at $\tilde{v} > 2$ is almost entirely removed from the Chae sample which greatly reduces the leverage on f_{trip} . It is notable that the right columns of Figs. 15-18 of Chae (2024) all show a systematic excess of data above models in the range $1.5 \leq \tilde{v} \leq 2$, perhaps indicating a problem in the triple modelling.

Further progress in the WB gravity test will likely depend on improved constraints and understanding of the triple population: in a first step in this direction, Manchanda et al. (2023) have shown that combining acceleration signals from the 10-year *Gaia* data plus followup speckle imaging and/or coronagraphic imaging will be able to detect almost all triples with a main-sequence third star at any separation. (Triples with a brown dwarf third object are much more challenging).

5. CONCLUSIONS

We have used a sample of wide binaries selected from *Gaia* DR3 to perform a test of a specific MOND model (with external field effect) against GR/Newtonian gravity. This includes a number of refinements from our earlier study in PS23, including several new selection cuts to discriminate against hierarchical triples; a wider range of r_p in the analysis; updates to the triple model with more realistic mass and semi-major axis distributions; velocity-averaging for short-period inner orbits;

and an improved fitting procedure which simultaneously fits multiple r_p bins with a flexible triple fraction f_{trip} plus unbound flyby and random-projection populations.

With our baseline triple model, the results show a rather strong preference for Newtonian gravity over the MOND model in question: this preference is robust against several variations on the baseline fit. The implied residual triple fraction is $f_{\text{trip}} \simeq 18.5$ percent (after the cuts to reject most triples). The implied triple fraction *before* our triple-rejection cuts with `ruwe`, `ipd_frac_multi_peak`, faint companion and Lobster cuts is approximately 37 percent, lower than the 63 percent inferred by the fit of Banik et al. (2024); this appears reasonable based on the formation model of Kouwenhoven et al. (2010).

We cannot claim that MOND is fully ruled out as yet: while our triple model is based on observational estimates, there remains a possibility that an alternative triple model may result in a lower triple fraction and/or a less poor fit to MOND. However, this seems unlikely for two reasons: first, we note that our triple model went through a number of upgrades during the course of this work: all our earlier iterations also preferred Newtonian gravity over MOND with fairly high $\Delta\chi^2$; so the triple model has been refined to match recent parameter estimates in the literature, but has not been fine-tuned to prefer Newtonian gravity. Second, it may be observed in Figure 10 for the MOND fits, the contributions from *binaries alone* are already tending high compared to the data at $0.8 \leq \tilde{v} \leq 1.2$ in the upper few r_p bins. Since the triple and other contributions cannot be negative, and in practice the triples must be significantly positive in this region in order to fit the tail at $\tilde{v} > 1.5$, reasonable modifications of the triple distribution will not remove this mismatch.

There are good prospects for improving this test: the upcoming *Gaia* DR4 release in 2026 will provide dramatically improved proper-motion precision, allowing expanding the sample to $G \sim 18$ and distance ~ 400 pc for improved statistics. The full-epoch astrometric data will also allow fitting for accelerations from long-period inner orbits, though the full power of this test will need to wait for the 10-year *Gaia* DR5 around 2030, as modelled in Manchanda et al. (2023). In the medium term future, combining the improvements from *Gaia* DR4/DR5 with additional followup to directly detect most triples and improve the constraints on the triple/quadruple population, there are excellent prospects for the wide-binary gravity test to become decisive.

ACKNOWLEDGEMENTS

We thank Indranil Banik and Kyu-Hyun Chae for many helpful discussions, and we thank two anonymous referees for comments which improved the paper. We thank the great effort of the *Gaia* DPAC team for the exceptional quality of the data. We have used the Python packages Numpy, Scipy, Matplotlib, Astropy, Lmfit, and Scikit-learn.

DATA AVAILABILITY

The original data used in this paper is publicly available. The *Gaia* data can be retrieved through the *Gaia* archive (<https://gea.esac.esa.int/archive>).

REFERENCES

- Andrews, J. J., Chanamé, J., & Agüeros, M. A. 2017, *MNRAS*, **472**, 675
- Banik, I., Pittordis, C., Sutherland, W., et al. 2024, *MNRAS*, **527**, 4573
- Banik, I. & Zhao, H. 2018, *MNRAS*, **480**, 2660
- Belokurov, V., Penoyre, Z., Oh, S., et al. 2020, *MNRAS*, **496**, 1922
- Benisty, D., Evans, N. W., & Davis, A.-C. 2023, *MNRAS*, **518**, L51
- Chae, K.-H. 2023, *ApJ*, **952**, 128
- Chae, K.-H. 2024, *ApJ*, **972**, 186
- Clarke, C. J. 2020, *MNRAS*, **491**, L72
- Creevey, O. L., Sordo, R., Pailler, F., et al. 2023, *A&A*, **674**, A26
- El-Badry, K. & Rix, H.-W. 2018, *MNRAS*, **480**, 4884
- El-Badry, K., Rix, H.-W., & Heintz, T. M. 2021, *MNRAS*, **506**, 2269
- Ester, M., Kriegel, H.-P., Sander, J., & Xu, X. 1996
- Famaey, B. & McGaugh, S. S. 2012, *Living Rev. Relativ.*, **15**, 10
- Fitton, S., Tofflemire, B. M., & Kraus, A. L. 2022, *Research Notes of the American Astronomical Society*, **6**, 18
- Gaia Collaboration, Prusti, T., de Bruijne, J. H. J., et al. 2016, *A&A*, **595**, A1
- Gaia Collaboration, Vallenari, A., Brown, A. G. A., et al. 2023, *A&A*, **674**, A1
- Hartman, Z. D., Lépine, S., & Medan, I. 2022, *ApJ*, **934**, 72
- Hernandez, X. 2023, *MNRAS*, **525**, 1401
- Hernandez, X., Chae, K.-H., & Aguayo-Ortiz, A. 2024a, *MNRAS*, **533**, 729
- Hernandez, X., Cookson, S., & Cortés, R. A. M. 2022, *MNRAS*, **509**, 2304
- Hernandez, X., Jiménez, A., & Allen, C. 2014, in *Accelerated Cosmic Expansion*, Vol. 38, 43
- Hernandez, X., Jiménez, M. A., & Allen, C. 2012a, in *Journal of Physics Conference Series*, Vol. 405, *Journal of Physics Conference Series*, 012018
- Hernandez, X., Jiménez, M. A., & Allen, C. 2012b, *EPJ C*, **72**, 1884
- Hernandez, X., Vereteletskiy, V., Nasser, L., & Aguayo-Ortiz, A. 2024b, *MNRAS*, **528**, 4720
- Hwang, H.-C., Ting, Y.-S., & Zakamska, N. L. 2022, *MNRAS* [2111.01789]
- Jiang, Y.-F. & Tremaine, S. 2010, *MNRAS*, **401**, 977
- Klüter, J., Bastian, U., & Wambsganss, J. 2020, *A&A*, **640**, A83
- Kouwenhoven, M. B. N., Goodwin, S. P., Parker, R. J., et al. 2010, *MNRAS*, **404**, 1835
- Kroupa, P., Weidner, C., Pflamm-Altenburg, J., et al. 2013, in *Planets, Stars and Stellar Systems. Volume 5: Galactic Structure and Stellar Populations*, ed. T. D. Oswalt & G. Gilmore, Vol. 5, 115
- Lépine, S. & Bongiorno, B. 2007, *AJ*, **133**, 889
- Lindgren, L., Klioner, S. A., Hernández, J., et al. 2021, *A&A*, **649**, A2
- Manchanda, D., Sutherland, W., & Pittordis, C. 2023, *The Open Journal of Astrophysics*, **6**, E2
- McGaugh, S., Lelli, F., & Schombert, J. 2016, *Phys. Rev. Lett.*, **117**, 201101
- Offner, S. S. R., Moe, M., Kratter, K. M., et al. 2023, in *Astronomical Society of the Pacific Conference Series*, Vol. 534, *Protostars and Planets VII*, ed. S. Inutsuka, Y. Aikawa, T. Muto, K. Tomida, & M. Tamura, 275
- Pecaut, M. J. & Mamajek, E. E. 2013, *ApJS*, **208**, 9
- Pedregosa, F., Varoquaux, G., Gramfort, A., et al. 2011, *Journal of Machine Learning Research*, **12**, 2825
- Penoyre, Z., Belokurov, V., & Evans, N. W. 2022, *MNRAS*, **513**, 2437
- Pittordis, C. & Sutherland, W. 2018, *MNRAS*, **480**, 1778
- Pittordis, C. & Sutherland, W. 2019, *MNRAS*, **488**, 4740
- Pittordis, C. & Sutherland, W. 2023, *The Open Journal of Astrophysics*, **6**, 4
- Riello, M., De Angeli, F., Evans, D. W., et al. 2021, *A&A*, **649**, A3
- Schubert, E., Sander, J., Ester, M., Kriegel, H., & Xu, X. 2017, *ACM Transactions on Database Systems*, **42**, 1
- Tokovinin, A. 2014, *AJ*, **147**, 87
- Tokovinin, A. 2023, *AJ*, **165**, 180
- Tokovinin, A. & Kiyaveva, O. 2016, *MNRAS*, **456**, 2070
- van Leeuwen, F., de Bruijne, J., Babusiaux, C., et al. 2022, *Gaia DR3 documentation*, *Gaia DR3 documentation*, European Space Agency; *Gaia Data Processing and Analysis Consortium*. Online at <https://gea.esac.esa.int/archive/documentation/GDR3/index.html>

APPENDIX

SQL QUERY

The following is the SQL query used to select the initial single-star dataset from the *Gaia* archive.

```

SELECT
gaiadr3.gaia_source.*,
gaiadr3.astrophysical_parameters.radius_flame,
gaiadr3.astrophysical_parameters.radius_flame_lower,
gaiadr3.astrophysical_parameters.radius_flame_upper,
gaiadr3.astrophysical_parameters.lum_flame,
gaiadr3.astrophysical_parameters.lum_flame_lower,
gaiadr3.astrophysical_parameters.lum_flame_upper,
gaiadr3.astrophysical_parameters.mass_flame,
gaiadr3.astrophysical_parameters.mass_flame_lower,
gaiadr3.astrophysical_parameters.mass_flame_upper,
gaiadr3.astrophysical_parameters.gravredshift_flame,
gaiadr3.astrophysical_parameters.gravredshift_flame_lower,
gaiadr3.astrophysical_parameters.gravredshift_flame_upper,
gaiadr3.astrophysical_parameters.flags_flame
FROM
gaiadr3.gaia_source
LEFT OUTER JOIN
gaiadr3.astrophysical_parameters
ON
gaiadr3.astrophysical_parameters.source_id
= gaiadr3.gaia_source.source_id

```

```
WHERE
gaiadr3.gaia_source.parallax >= (10.0/3.0)
AND
gaiadr3.gaia_source.phot_g_mean_mag <=17
AND
(ABS(gaiadr3.gaia_source.b) >= 15)
ORDER BY
gaiadr3.gaia_source.dec ASC
```